Astronomy & Astrophysics manuscript no. output
November 11, 2026
©ESO 2026

Euclid Data Release (DR1)

NIR astrometric calibration

Euclid Collaboration: M. Radovich, R. da Silva, G. Polenta, A. Alavi, H. Aussel, P. Awad, A. Bonchi, L. Bramante, et al.

(Full author list and affiliations details can be found after the references)

November 11, 2026

ABSTRACT

This paper presents the methodology and results of the astrometric calibration applied to the *Euclid* Near-Infrared (NIR) images in the Euclid Data Release 1, focusing on the techniques used to model and correct instrumental distortions, as well as the assessment of calibration quality. This work details the calibration pipeline, including quality control tests, and the evaluation of astrometric residuals against the *Gaia* DR3 catalogue and internal consistency metrics based on data encompassing more than one year of *Euclid* operation: the achieved accuracy is 30 mas for 97% of the total area, thus exceeding the requirements for Data Release 1. For the remaining 3%, accuracy declines due to a persistence correction issue: a method to correct the issue is presented. Furthermore, we discuss the stability of the solution over time, its dependence on source properties and instrument configuration, and outline the improvements planned for future *Euclid* data releases to enhance the astrometric calibration accuracy and efficiency.

Key words. Cosmology: observations – Surveys – Astrometry – Techniques: image processing – Space vehicles: instruments – Instrumentation: detectors

1. Introduction

Accurate astrometric calibration is essential for the success of the *Euclid* mission (Euclid Collaboration: Mellier et al. 2025), which enables the precise mapping of celestial sources across its detectors. The astrometric calibration process ensures the reliable alignment of observed images with external reference catalogues, such as *Gaia* DR3 (Gaia Collaboration: Vallenari et al. 2023), and maintains internal consistency among multiple dithered images. *Euclid*'s Near-Infrared Spectrometer and Photometer (NISP: Euclid Collaboration: Jahnke et al. 2025) features three imaging channels: $Y_{\rm E}$, $J_{\rm E}$, and $H_{\rm E}$. An array of 16 HAWAII-2RG (H2RG) detectors, each with 2048x2048 pixels and a plate scale of $0\farcs3$ pixel^{-1}, provides a field of view of 0.57 deg^2. We recall that within *Euclid*, a dithering sequence operating mode is termed a single observation, and the individual exposures (dithers) of each observation are archived under an Observation ID (`OBSID` hereafter). In the wide survey, each `OBSID` consists of four dithers; the self-calibration field consists of 76 dithers (Euclid Collaboration: Mellier et al. 2025; Euclid Collaboration: Polenta et al. 2026b). In DR1 (Euclid Data Release 1 2026), NISP calibrated images and associated catalogues are available for both single dithers and stacked products (Euclid Collaboration: Polenta et al. 2026a).

For the initial data releases (DR1 and DR2), the astrometric calibration requirement is set as a root mean square (RMS) of 200 mas for both RA and Dec, compared to the external reference (absolute astrometry), and 100 mas for the positions of the same sources observed within a dither sequence (relative astrometry). The ultimate aim of the final release (DR3) is to achieve an RMS of 30 mas on each axis for both relative and absolute astrometry, corresponding to 0.1 pixels. An additional requirement pertains to geometric distortion, which must be calibrated to within 0.015% over scales of 3 arcmin. This paper focuses on the methods used to model and correct instrumental distortions in images from the NISP photometric channel (NISP-P) and assesses the calibration quality achieved in the Euclid DR1, covering an area of 1900 deg^2 (Euclid Collaboration: Scaramella et al. 2022). The paper is organized as follows. Section 2 summarises the astrometric calibration module of the NIR processing function (NIR-PF) pipeline and its quality control tests. Section 3 presents the results obtained in the DR1, evaluating astrometric residuals against external catalogues and internal consistency metrics based on more than 1 year of *Euclid* operations. This analysis shows that the astrometric calibration meets the requirements on the RMS and on the geometric distortion accuracy, described in Sect. 3.3. The stability of the astrometric solution over time and its dependence on source properties and instrument configuration are also discussed in Sect. 3.3. Section 4 outlines the enhancements already implemented for Euclid Data Release 2, as well as additional improvements that may further refine the calibration accuracy and efficiency in later data releases. To support the use of the calibrated data products, for each parameter described in the text we also give the corresponding keyword in the `NIR_AstrometricCalibration` module of the NIR-PF (`NIR_Astrometry` hereafter).

2. Astrometric calibration of NISP images in Euclid DR1

In the NIR-PF, `NIR_Astrometry` relies on the `Scamp`[1] software (Bertin 2006) to compute the distortion and update the associated keywords in the headers of the `FITS` frames. This is done

[1] The NIR-PF adopts a rengineered version of `Scamp`, named as `EL_ScampPP`.

for each dither, because the combined effect of the tilt in the NISP optics (Euclid Collaboration: Schirmer et al. 2022) and an offset of the filter centre from the optical axis, due to uncertainty in filter positioning, leads to variations in the distortion pattern that prevent us assuming a constant distortion across different exposures.

`Scamp` utilises the `PV` formalism (see e.g. Calabretta & Greisen 2002; Shupe et al. 2012), which calculates the distortion for each detector by mapping pixel coordinates (x, y) from that detector to intermediate world coordinates (ξ, η). The distortion is applied to the coordinates projected onto the focal plane as

$$X = C_{11}(x - p_x) + C_{12}(y - p_y)\,,$$
$$Y = C_{21}(x - p_x) + C_{22}(y - p_y)\,,$$
$$\xi = \sum_{m+n\leq N} a_{mn} X^m Y^n, \tag{1}$$
$$\eta = \sum_{m+n\leq N} b_{mn} X^m Y^n.$$

The relevant quantities are defined as follows: p_x and p_y are the coordinates of the reference pixel, corresponding to the `CRPIX` keywords in the `FITS` files; C_{ij} are the elements of the linear transformation matrix that accounts for pixel scale and rotation, stored in the `CD` keywords; and a_{mn} and b_{mn} are for each axis the coefficients of the polynomial with order N describing the distortion, corresponding to the `PV` keywords. In `NIR_Astrometry`, the distortion (Fig. 1) is represented by a polynomial with $N = 3$. This approach involves working in sky coordinates using a tangent-plane projection. In cases such as *Euclid*, where the detectors are not aligned with the celestial coordinates, the polynomial coefficients are dependent on the telescope rotation. In contrast, the `SIP` formalism (Shupe et al. 2005) describes the distortion directly in the focal plane without relying on the tangent-plane projection. It uses polynomial distortion coefficients A_{ij} and B_{ij} (often encoded as `SIP` keywords) to model the optical and instrumental distortions that affect the pixel coordinates on the detector and transform them into intermediate world coordinates:

$$u = x - p_x, \qquad v = y - p_y\,,$$
$$U = u + \sum_{i+j\leq N} A_{ij} u^i v^j, \qquad V = v + \sum_{i+j\leq N} B_{ij} u^i v^j\,, \tag{2}$$
$$\xi = C_{11}U + C_{12}V\,, \qquad \eta = C_{21}U + C_{22}V\,.$$

In this case, because the distortion is expressed purely in focal plane terms, it does not depend on the telescope rotation.

In DR1, the adopted external reference is the *Gaia* DR3 catalogue (Gaia Collaboration: Prusti et al. 2016; Vallenari 2022), which is also the reference catalogue adopted for the astrometric calibration of the VIS channel. The positions from the VIS catalogue are not utilised for the following reasons. (1) Although there is a significant overlap between the VIS and NISP coverage in each exposure, it is not complete; therefore, incorporating additional adjacent VIS fields becomes necessary, but these fields are not guaranteed to be observed. (2) Point sources brighter than I_E =18.5 are saturated in VIS normal exposures (Euclid Collaboration: McCracken et al. 2026); as a consequence, a significant fraction of bright sources that are not saturated in NISP[2] and

[2] In NISP, the saturation limit for bright sources is approximately 16.0 AB mag (Euclid Collaboration: Jahnke et al. 2025).

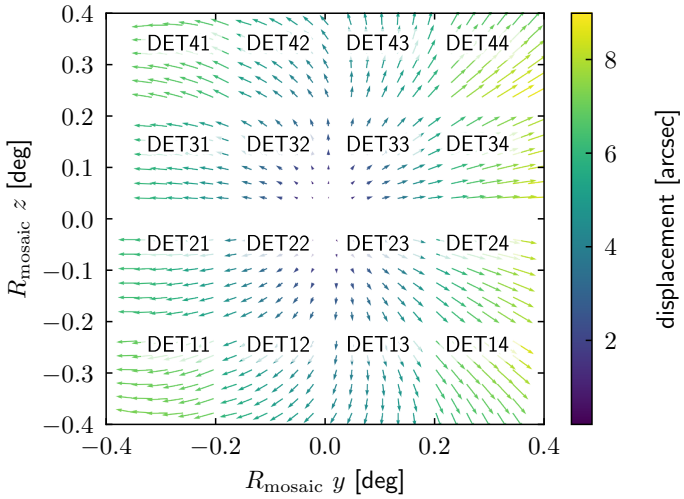


Fig. 1. Distortion map showing the displacement (arcsec) on the focal plane in the `R-mosaic` coordinate system (Euclid Collaboration: Jahnke et al. 2025), as derived from a self-calibration observation.

therefore available for astrometric calibration with *Gaia* DR3 as reference, would be saturated in VIS and thus not usable with VIS as reference.

The *Gaia* DR3 celestial coordinates (epoch J2016.0) are propagated to the Euclid dither epoch through the application of proper motions. The final Euclid calibrated positions are in the barycentric ICRS.

`Scamp` processes the catalogues generated by `SExtractor` (Bertin & Arnouts 1996) in combination with `PSFex` (Bertin 2011), optimising the precision of source centres through point-spread function (PSF) fitting. The implementation of PSF fitting in the NIR-PF is discussed in detail in Euclid Collaboration: da Silva et al. (2026). Within `Scamp`, the quality maps produced by the NIR-PF (Euclid Collaboration: Polenta et al. 2026b) enable the exclusion of sources that are either saturated or compromised by issues like cosmic rays and persistence. The sources used for astrometric calibration have *Gaia* DR3 magnitudes, G, in the 15 to 21 range, corresponding to approximately 16 to 22.5 in the NIR bands.

The robustness of astrometric calibration can be enhanced by supplying `Scamp` with an initial estimate of the distortion (presolution). This approach is particularly advantageous for the detectors at the edges of the field of view (Fig. 1), where distortion is more pronounced, thereby complicating the alignment with the external reference catalogue. In the current implementation, the presolution primarily serves as an initial input to `Scamp`, functioning as a preliminary estimate or starting point rather than delivering a highly precise outcome. In this implementation, because the presolution is primarily used to guide the matching of sources before further processing in `Scamp`, the demand for accuracy is relatively low (around 1″). Although the distortion pattern is expected to vary among different exposures, deriving the presolution once is sufficient for the intended purpose of the current implementation. This derivation is based on the observations of the self-calibration field. The presolution initially contains distortion terms expressed in the `Scamp PV` format, along with the values encoded in the `CD` and `CRPIX` keywords. To facilitate its application to observations with varying telescope rotation angles, the presolution is initially transformed into the `SIP` format. Subsequently, it is converted back to the PV format, with modifications made to the `CD` matrix terms to accommodate the instrument rotation. Analytical expressions derived using the

sympy package in Python are applied for all conversions between the PV and SIP formats. At this point, there may be an offset in the celestial coordinates of the tangent-point, defined by the CRVAL keyword in the images. Although Scamp corrects this offset before calculating the distortion, it is ineffective in situations such as a Fine Guidance Sensor (FGS) failure, which results in elongated source images, or when cosmic ray showers impact a significant number of pixels, necessitating the exclusion of the exposures regardless. Consequently, NIR_Astrometry initially employs Scamp exclusively to adjust the CRVAL values, followed by an initial alignment utilising the *Gaia* DR3 catalogue through the presolution. Subsequently, a series of tests is conducted for each dither, to identify those for which it is not possible to derive a reliable astrometric solution.

- If the median ellipticity of the matched sources (ASTRELL keyword) exceeds a threshold of $\epsilon_{\rm th} = 0.3$ or is more than twice the median across all dithers, it is highly likely that the dither is compromised owing to a failure in the FGS.
- If a detector records an abnormally low number of detections (< 5) or if the fraction of matched sources is too low compared to those in the external catalogue ($< 10\%$), it becomes impossible to reliably estimate the distortion.

The threshold values mentioned above are selected based on an analysis of a subset of dithers with known issues and may be refined in future data releases. For the dithers that successfully pass these evaluations, Scamp is executed once more to calculate the total distortion. One-third of the dithers identified as invalid in the NIR-PF (Euclid Collaboration: Polenta et al. 2026a) are marked as such through this step. Section 3.1 presents an overview of the astrometric calibration results for dithers that pass the validity tests.

3. Analysis of astrometric residuals

We present a summary of the astrometric residuals generated by NIR_Astrometry, both in relation to the *Gaia* DR3 catalogue and internally among the dithers. To accomplish this, we select 4000 OBSID from the Euclid Wide Survey in the Science Archive System (SAS) for each NISP filter, covering an area of 1950 deg^2 after removing overlaps (Sect. 3.2.4), over more than 1 year of operation (from February 2024 to May 2025).

To assess the quality of the astrometric calibration, we use the following quantities derived from the positional differences between the N detections and their matched reference sources, $\Delta\alpha^*_i = (\alpha_i - \alpha_{{\rm ref},i})\cos\delta_{{\rm ref},i}$ in right ascension (RA) and $\Delta\delta_i = \delta_i - \delta_{{\rm ref},i}$ in declination (Dec). Quantities in RA marked with an asterisk indicate that they are multiplied by $\cos\delta$ to measure angular distances on the sky.

Average offset. The mean positional difference, which indicates the calibration bias, is given by

$$\langle\Delta\alpha^*\rangle = \frac{1}{N}\sum_{i=1}^{N}\Delta\alpha^*_i\,, \quad \langle\Delta\delta\rangle = \frac{1}{N}\sum_{i=1}^{N}\Delta\delta_i\,. \tag{3}$$

Standard deviation (σ). This measures the spread of the positional offsets around the mean, thereby indicating the calibration precision,

$$\sigma^2_{\alpha^*} = \frac{1}{N}\sum_{i=1}^{N}\left(\Delta\alpha^*_i - \langle\Delta\alpha^*\rangle\right)^2\,, \quad \sigma^2_{\delta} = \frac{1}{N}\sum_{i=1}^{N}\left(\Delta\delta_i - \langle\Delta\delta\rangle\right)^2\,. \tag{4}$$

RMS offset. This is the square root of the mean squared positional differences, representing the total calibration accuracy (bias + precision),

$$\mathrm{RMS}^2_{\alpha*} = \frac{1}{N}\sum_{i=1}^{N}(\Delta\alpha^*_i)^2\,, \quad \mathrm{RMS}^2_{\delta} = \frac{1}{N}\sum_{i=1}^{N}(\Delta\delta_i)^2\,. \tag{5}$$

Where the RMS or σ represents the sum over both coordinates, it is expressed as $\mathrm{RMS}^2 = \left(\mathrm{RMS}^2_{\alpha*} + \mathrm{RMS}^2_{\delta}\right)/2$.

In NIR_Astrometry, the average offset relative to the reference catalogue is produced as an output and stored in the headers of the calibrated images using the keywords ASTROFF1 and ASTROFF2, corresponding to the RA and Dec coordinates, respectively. The keywords ASTIRMS1, ASTIRMS2 represent the standard deviation of the residuals for sources matched across different dithers; ASTRRMS1, and ASTRRMS2 refer to those compared to the reference catalogue. They are computed both for single detectors and the entire dither. Given that the average offset in each detector or dither is negligible, the standard deviation matches the RMS of the deviations. During the validation process, dithers are flagged if any value of ASTIRMS1, ASTIRMS2, ASTRRMS1, or ASTRRMS2 computed throughout the entire dither exceed 50 mas or if ASTRIRMS1 or ASTIRMS2 exceed 50 mas in any detector.

3.1. Astrometric residuals in dithers

Figure 2 illustrates the distribution of average ellipticities, the number of matches with *Gaia* DR3 sources, and the residuals (offsets and standard deviations) in both the dithers (upper and middle rows) and individual detectors (bottom row). This confirms that, as anticipated in Sect. 3, the average offset to the reference catalogue is indeed negligible, being within 2 mas; the astrometric calibration accuracy is approximately 10 mas and remains below 20 mas for 99% of the dithers, in all bands. The RMS decreases from $Y_{\rm E}$ to $J_{\rm E}$ and $H_{\rm E}$, consistent with the stronger undersampling of the diffraction-limited PSF at shorter wavelengths (Euclid Collaboration: Jahnke et al. 2025; Euclid Collaboration: da Silva et al. 2026). For individual detectors, mostly DET13 and DET14, a small fraction exhibits a standard deviation exceeding 60 mas and potentially reaching up to 150 mas. This fraction is at most 0.15% for $H_{\rm E}$ and is even lower in the other bands. As discussed in more detail in Sects. 3.6 and 4.1, the problem was identified as stemming from an excessively stringent exclusion of detections linked to the persistence flagging.

Figure 2 also confirms that, among the dithers that passed the initial selection, the average ellipticity is less than 0.16. In future data releases, a threshold lower than the current value ($\epsilon_{\rm th} = 0.3$) could be chosen to identify dithers affected by the FGS issue.

3.2. Analysis of stacked catalogues

To comprehensively assess the accuracy and robustness of the astrometric calibration of NIR images in the Euclid DR1, we present a series of diagnostic tests performed to investigate potential dependencies affecting the residuals. These tests examine variations in astrometric residuals as a function of Galactic extinction, source colour, observation time, and telescope rotation. Additionally, internal consistency checks analyse offsets between different filters and between the NISP and VIS bands, as well as comparisons with the *Gaia* DR3 catalogue. To accomplish this, we examine the stacked catalogues produced for

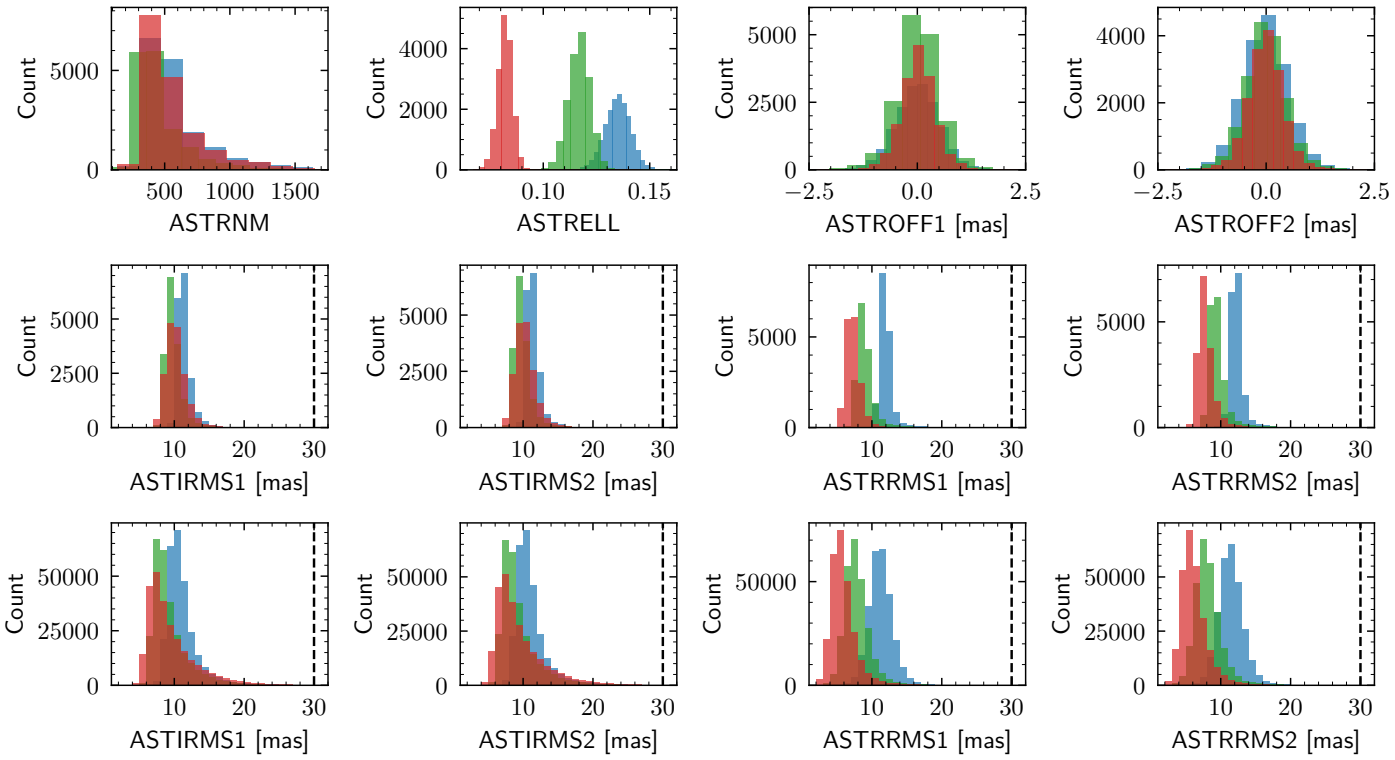


Fig. 2. Histograms illustrating the following for each of the $Y_{\rm E}$ (blue), $J_{\rm E}$ (green), and $H_{\rm E}$ (red) filters: the number of matched sources available for astrometric calibration (`ASTRNM`); the median ellipticity (`ASTRELL`); the average offsets (`ASTROFF1`, `ASTROFF2`); the standard deviations of residuals for sources matched across dithers (`ASTIRMS1`, `ASTIRMS2`), and compared to the reference catalogue (`ASTRRMS1`, `ASTRRMS2`). The top two rows pertain to dithers, while the bottom row corresponds to values within individual detectors. The dashed line represents the final requirement for the RMS, set at 30 mas.

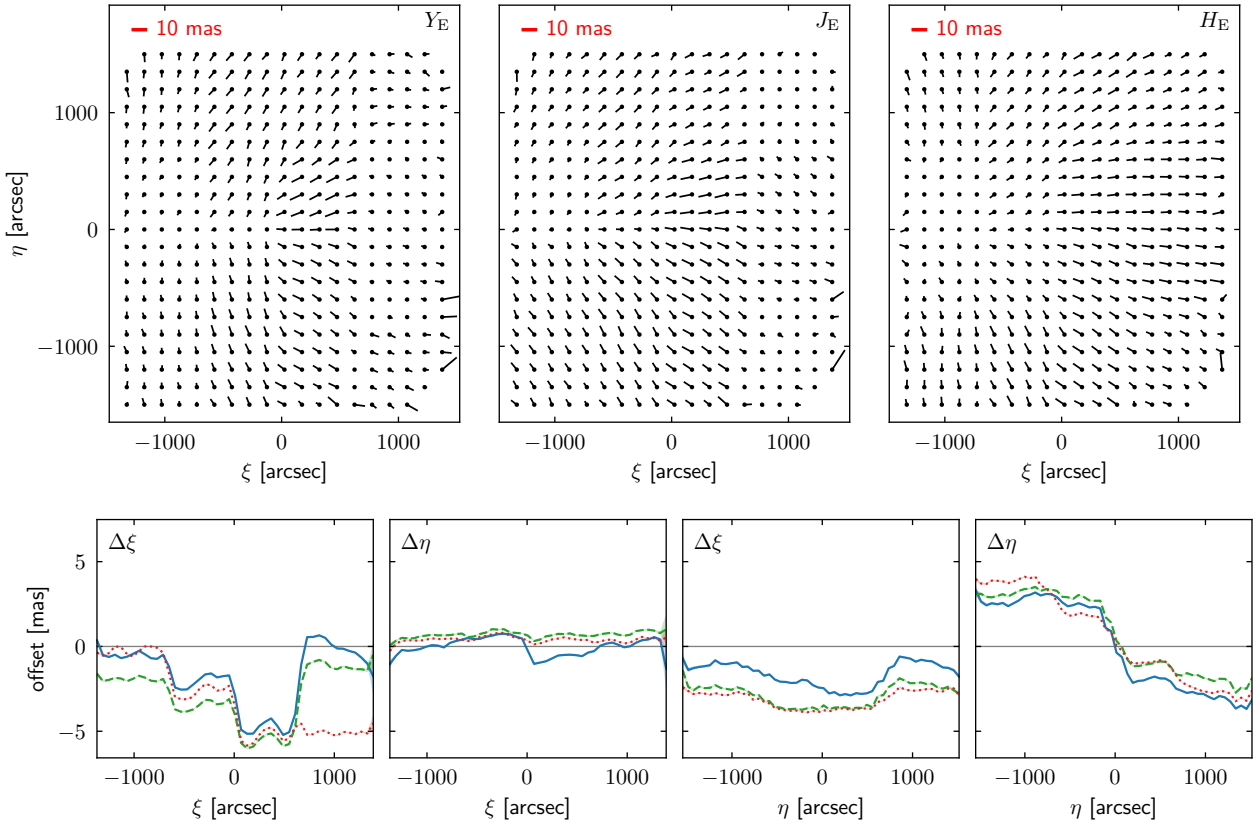


Fig. 3. Clipped mean astrometric residuals in the instrument frame, obtained combining the measurements from the stacked catalogues. Top: whiskers with components $(\langle\Delta\xi\rangle, \langle\Delta\eta\rangle)$ derived in 2.′5 × 2.′5 cells. Bottom: $\Delta\xi$ and $\Delta\eta$ as a function of ξ and η for $Y_{\rm E}$ (blue), $J_{\rm E}$ (green), and $H_{\rm E}$ (red).

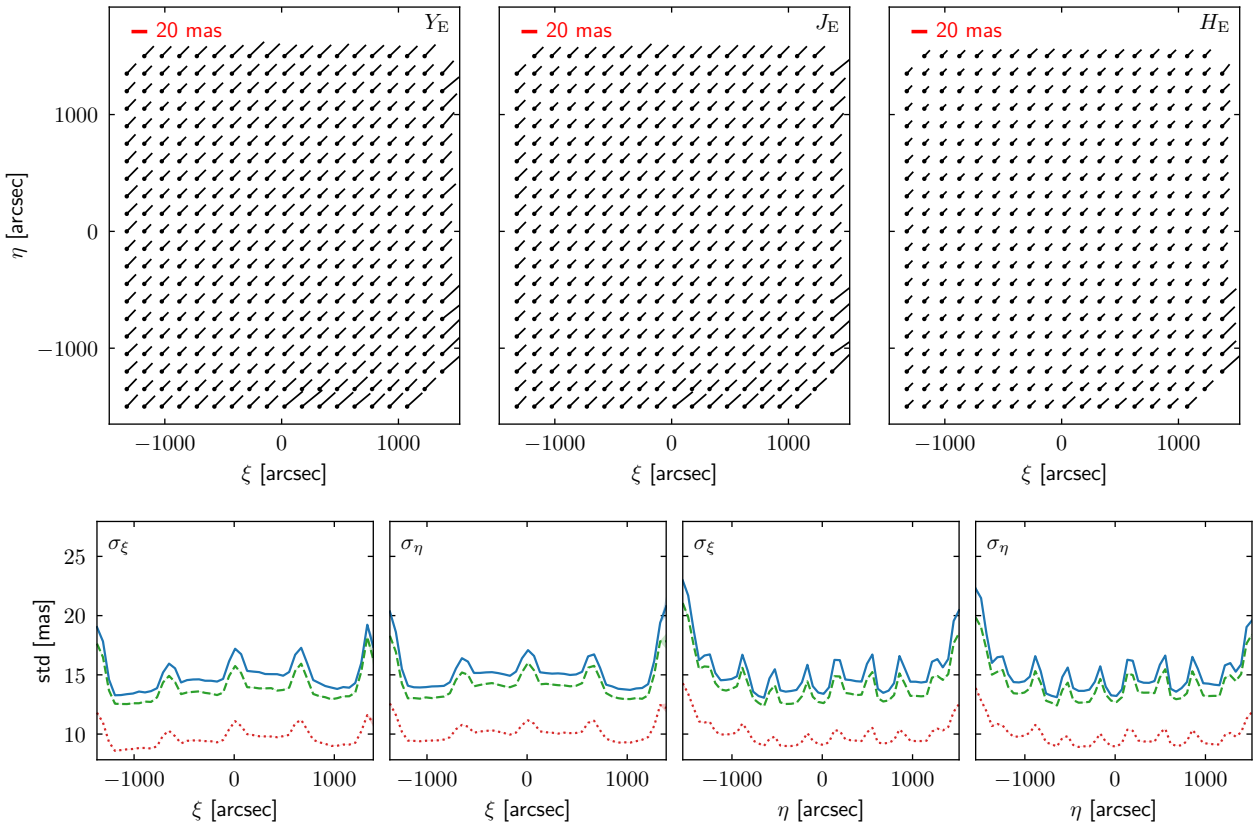


Fig. 4. As in Fig. 3, but for the standard deviation of the residuals. Whiskers have components (σ_ξ, σ_η). The increased residuals at the edges results from the dithering pattern, which reduces the number of dithers in those areas.

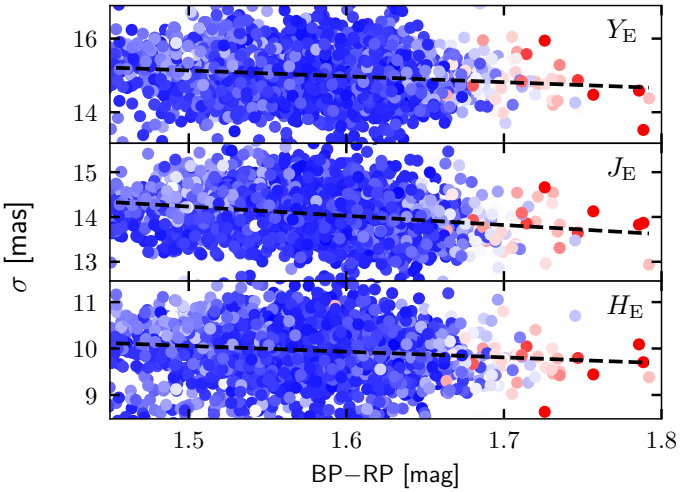


Fig. 5. Standard deviation of the residuals in each stacked catalogue, summed in quadrature on α and δ. This is displayed in relation to the average *Gaia* DR3 colours of the matched sources. The Galactic extinction is represented by the colours: bluer hues indicate lower Galactic extinction, whereas redder hues correspond to higher values. The linear fit, depicted as a dashed line, has a slope of less than 3 mas mag^{-1} across all bands.

each OBSID rather than single dithers. Consequently, the results are independent of those derived from individual dithers during the astrometric calibration. A comparison of the residuals from the *Gaia* DR3 positions obtained on dithers in NIR_Astrometry and those from the stacked catalogues reveals consistency, with a median standard deviation (σ_α, σ_δ) of approximately 10 mas, and 95% of the dithers falling within 15 mas.

The centroids of the sources in the stacked catalogues, obtained by PSF-fitting (Euclid Collaboration: Polenta et al. 2026b), are cross-matched with the *Gaia* DR3 catalogue by applying the selection criteria described in Sect. 2. A strict mutual nearest-neighbour algorithm is adopted in the cross-match to minimise duplicate or incorrect assignments. First, we perform a forward match, identifying the nearest *Gaia* DR3 source for each target object in the stacked catalogue. Next, we perform a reverse match, identifying the nearest target object for every source in the *Gaia* DR3 catalogue. A cross-match is considered if two criteria are met: (1) the target object and the *Gaia* DR3 source are each other's closest reciprocal matches; and (2) their angular separation does not exceed a maximum tolerance of 1″.

3.2.1. Astrometric residuals versus position angle and time

In the PV formalism, distortion changes with the instrument's rotation relative to the sky. To test whether the position-angle-dependent distortion model introduces spurious residuals, we fitted, for each band, the RMS of the residuals per observation and their mean offsets in the instrument frame ($\Delta\xi$, $\Delta\eta$) with a sinusoidal function of the position angle. The amplitude of the sinusoid is 0.08–0.14 mas for the RMS, compared with a median RMS of approximately 10 mas per observation, and at most 0.08 mas for the mean offsets, compared with their uncertainty of 0.5–0.8 mas per observation. The position-angle dependence of the distortion model therefore introduces no significant spurious residuals. Similarly, a linear fit of the RMS per observation as a function of time gives slopes of 0.04–0.11 mas yr^{-1}, i.e. a

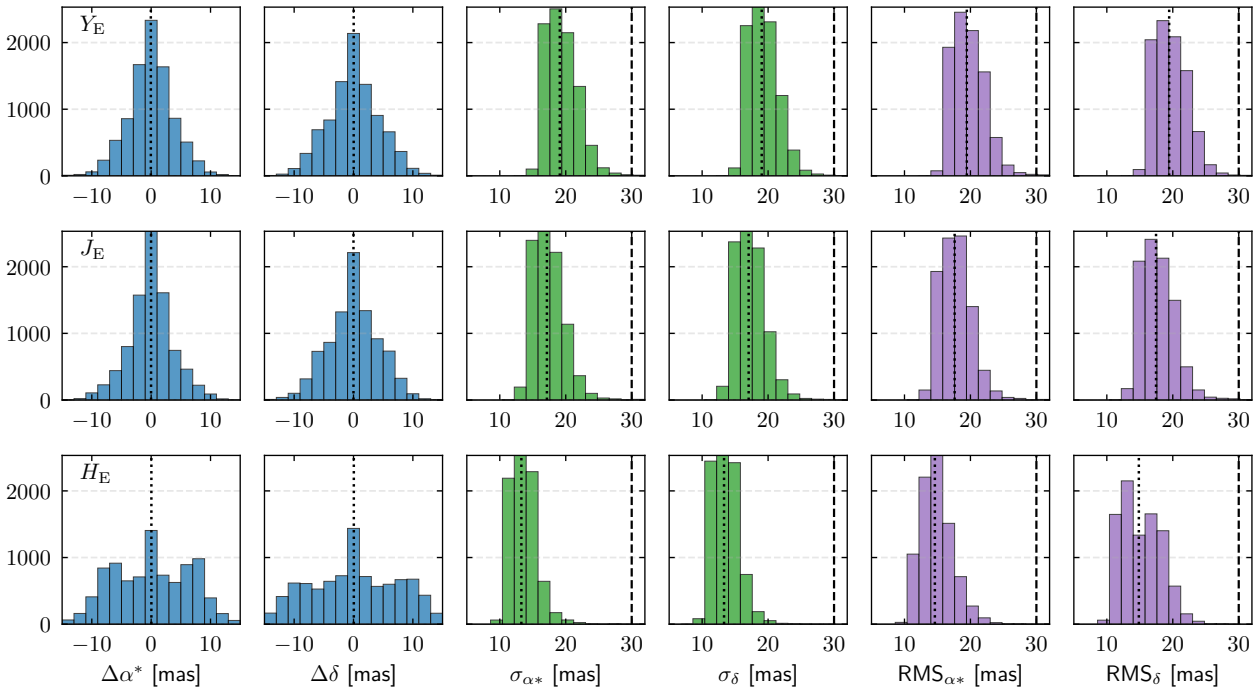


Fig. 6. Distribution of astrometric residuals, including median offsets, standard deviations σ, and RMS, is displayed in the overlaps across the stacked catalogues. For the plots displaying σ and RMS, the dashed line represents the legacy requirement (30 mas). Vertical dotted lines indicate the median values.

change of at most 0.2 mas over the period covered by the observations, which is again negligible.

3.2.2. Astrometric residuals versus focal plane position

To examine the discrepancies across the focal plane, we create an astrometric residual map for each filter. For this purpose, we first collect from all stacked catalogues the detections matched with *Gaia* DR3. When averaging frames with different rotations, offsets are diluted if derived from sky coordinates. For this reason here we compute offsets from the reference pixel (u, v in Eq. 2) converted to arcseconds with the pixel scale (ξ, η), and derive the NISP−*Gaia* DR3 residuals in the instrument frame ($\Delta\xi$, $\Delta\eta$). Since the scatter is nearly isotropic, the RMS is instead frame invariant ($\sigma_\xi \sim \sigma_{\alpha*}$, $\sigma_\eta \sim \sigma_\delta$) .

The mean offsets and the scatter of the residuals $\Delta\xi$ and $\Delta\eta$ are computed from the combined detections of all stacked catalogues, as a function of the position ξ, η in the stack frame. For the two-dimensional maps (Figs. 3 and 4, top rows), the (ξ, η) plane is divided into non-overlapping cells of $2.5' \times 2.5'$, each containing on average 10^4 detections. In each cell, the mean and the standard deviation of $\Delta\xi$ and $\Delta\eta$ are computed after an iterative 3σ clipping of all the detections falling in it; cells with fewer than 100 detections after clipping are discarded. Each cell is represented by a whisker starting at the cell centre: its components are $\langle\Delta\xi\rangle$ and $\langle\Delta\eta\rangle$ for the mean offsets, and σ_ξ and σ_η for the scatter. To highlight trends along each axis, we also compute one-dimensional profiles (Figs. 3 and 4, bottom rows) in independent strips $1'$ wide, running along ξ and η across the whole field, each containing on average 10^5 detections; the same 3σ-clipped statistics are applied. As a result of this analysis, across the focal plane offsets are below ±5 mas in all bands; the standard deviation in both ξ and η does not vary significantly and, consistently with previous results, decreases from Y_E, J_E (∼ 15 mas) and H_E (∼ 10 mas).

3.2.3. Astrometric residuals versus source colour

Figure 5 illustrates the standard deviations of the astrometric residuals measured in each stacked catalogue, as a function of the average *Gaia* DR3 BP − RP colours, with average redder colours corresponding to a higher Galactic extinction. A slight trend is noticeable, with a difference of less than 1 mas between stacks with average bluer and redder colours. A correlation between astrometric residuals and average source colours would be expected in the case of chromaticity effects in the PSF, where the measured centroid would be expected to vary with stellar colour and increase the astrometric scatter. A higher Galactic extinction shifts the selected *Gaia* DR3 stars towards redder colours and narrows the colour distribution: in the case of a PSF chromaticity, this would result in a smaller PSF variation across the sample than in fields with a low Galactic extinction, thus reducing the chromatic contribution to the astrometric scatter. A slight trend is noticeable, with a difference of less than 1 mas between stacks at lower and higher extinction levels. To further verify whether the astrometric calibration may be influenced by chromaticity effects, we examine the correlations between the residuals along the x and y axes of the detectors and *Gaia* DR3 colours (BP − RP). For this purpose, *Gaia* DR3 positions and those measured in the NISP stacks are first reprojected onto the focal plane, and the residuals along the detector axes ($\Delta\xi$, $\Delta\eta$) are computed and binned in BP − RP colours. The chromaticity terms, represented as R_ξ and R_η, are defined as the slopes of these binned residuals against BP − RP: $R_\xi = \langle\Delta\xi\rangle_{\rm bin} / (\mathrm{BP}-\mathrm{RP})_{\rm bin}$, $R_\eta = \langle\Delta\eta\rangle_{\rm bin} / (\mathrm{BP}-\mathrm{RP})_{\rm bin}$ are finally derived. We find that for all filters, $R_\xi < 1$ mas mag^{-1} and $R_\eta \ll 1$ mas mag^{-1}.

3.2.4. Astrometric consistency across overlaps

Stacks of adjacent observations may overlap. This overlap enables us to assess whether the astrometric calibration remains consistent for the same sources that are detected in different

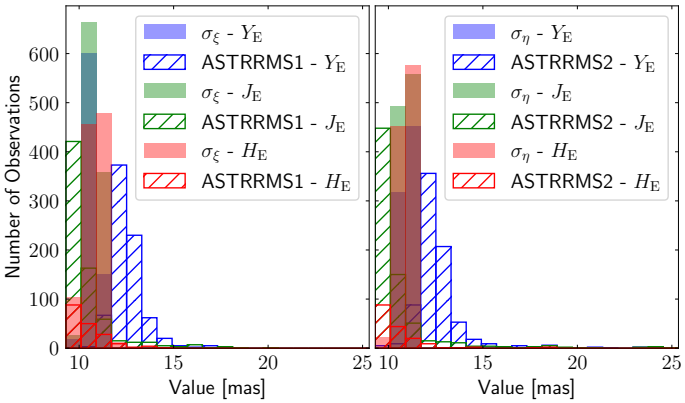


Fig. 7. Comparison of the standard deviation of residuals when evaluating the impact of distortion calculated using `Scamp` versus a fixed distortion across the three NISP bands, in the self-calibration dithers. The hashed areas represent the standard deviations of residuals using the *Gaia* DR3 catalogue as a reference, computed with `NIR_Astrometry`; the filled areas correspond to the values derived from the procedure outlined in the text, which assumes a constant distortion while varying only the linear terms.

stacks. To accomplish this, we select pairwise overlaps between stacks, with each having an overlap of at least 50 arcmin^2, ensuring sufficient detections for a meaningful analysis. This results in a total area of 560 deg^2. As shown in Fig. 6, for 99% of the overlaps the standard deviation in both coordinates remains within 25 mas, while the median offsets are within 10 mas. This is in agreement with what derived in the previous sections.

3.3. Geometric distortion: accuracy and stability

We verify whether the geometric distortion is calibrated within 0.015% over scales of 3′, as in the requirement. To achieve this, for each stacked catalogue we extract within the matched sources the pairs separated by a distance $d_{\rm ref}$ between 2.′5 and 3.′5 in the *Gaia* DR3 catalogue, used as the reference. We then compare these pairs with the corresponding ones in the Y_E, J_E, and H_E catalogues, where the separation is $d_{\rm NIR}$, resulting in the fraction $\nu = |d_{\rm ref} - d_{\rm NIR}|/(\sqrt{2}d_{\rm ref})$. A factor of $\sqrt{2}$ is introduced to transform pair separations into single-source equivalents. In all the stacks examined here, the RMS of ν is less than 0.01%; in each stack, 95% of the considered pairs have $\nu < 0.02\%$. To ensure that this test accurately traces geometric distortions without being influenced by random centroiding noise, we conduct the analysis again on a 15″ scale, where the impact of geometric distortion is minimal, and find the noise contribution to be negligible.

We then evaluate how well the assumption of a constant presolution aligns with the actual distortion observed in the dithers. For this purpose it is essential to separate the distortion, assumed to be constant, from the components that may vary across different observations: here we assume that they may be described by offset and linear terms. This is performed using a set of artificial source positions, following the procedure outlined below.

1. A list of artificial sources positioned on a grid (x, y) that matches the detector's size of 2048×2048 pixels is created.
2. This list is transformed into intermediate world coordinates (IWC) using the `PV` distortion computed by `NIR_Astrometry`, yielding the reference coordinates $(\xi_{\rm r}, \eta_{\rm r})$.
3. The `PV` distortion model contained in the presolution is converted to `SIP`. Equation (2) is applied to transform pixel coordinates (x, y) to intermediate coordinates (U, V), using only the nonlinear terms of the `SIP` distortion ($i + j \geq 2$).
4. A least squares minimisation is performed to fit the C_{ij} terms of the `CD` matrix (Eq. 1) and an offset $(\Delta\xi, \Delta\eta)$:

$$\xi_{\rm r} = C_{11}U + C_{12}V + \Delta\xi\,; \qquad \eta_{\rm r} = C_{21}U + C_{22}V + \Delta\eta\,. \quad (6)$$

5. The offset $(\Delta\xi, \Delta\eta)$ is converted back to pixel offsets $(\Delta U, \Delta V)$ by applying the inverse `CD` matrix:

$$\Delta U = \frac{C_{22}\Delta\xi - C_{12}\Delta\eta}{|C|}\,; \qquad \Delta V = \frac{C_{11}\Delta\eta - C_{21}\Delta\xi}{|C|}\,. \quad (7)$$

   Here $|C| = C_{11}C_{22} - C_{12}C_{21}$. The offsets ΔU, ΔV replace the constant terms in the SIP polynomials, $A_{0,0}$ and $B_{0,0}$. Because the linear terms are now represented by the fitted `CD` matrix, the linear `SIP` terms $A_{1,0}$, $A_{0,1}$, $B_{1,0}$, and $B_{0,1}$ are set to zero to avoid redundancy.
6. The reference coordinates $\xi_{\rm r}$, $\eta_{\rm r}$ are compared with the coordinates $\xi_{\rm n}$, $\eta_{\rm n}$ obtained by applying the new distortion terms.

We analyse 15 observations of the self-calibration field, each comprising 76 dithers with varying rotation angles. This selection is made because of the notably stable distortion observed in these cases. The $(\xi_{\rm n}, \eta_{\rm n})$ values obtained from the pixel grid are compared with those derived by applying the `Scamp` distortion contained in the headers $(\xi_{\rm r}, \eta_{\rm r})$, and the offsets are analysed. Figure 7 illustrates the comparison between the standard deviation of these offsets and those computed by `NIR_Astrometry` with respect to the *Gaia* DR3 sources (`ASTRRMS1`, `ASTRRMS2`), based on the `Scamp` processing. In both methods, the median of the standard deviations is approximately 10 mas, and within 20 mas for 99% of them. These findings suggest that the distortion remains consistently stable over time, within a margin of approximately 10 mas. However, they also imply that the assumption that linear components can sufficiently account for the residual variations in distortion may not hold true, as further discussed in Sect. 4.2.

3.4. Effect of stellar aberration and plate-scale stability

The *Gaia* DR3 reference positions used in the astrometric calibration are barycentric and are propagated to the epoch of each exposure using proper motions only; no correction for stellar aberration due to the motion of *Euclid* is applied. To first order, aberration changes the apparent angular separations across the field by a factor $(1 + \mathbf{v}\cdot\hat{\mathbf{n}}/c)$, where $\mathbf{v}$ is the barycentric velocity of *Euclid*, given by the `VEL_X`, `VEL_Y`, `VEL_Z` values in the frame headers, and $\hat{\mathbf{n}}$ the direction of the field, derived from the `CRVAL1` and `CRVAL2` values. Since the astrometric solution maps the observed pixel positions onto barycentric reference positions, this term is absorbed into the fitted plate scale s, which is then expected to vary by $\Delta s/s = \mathbf{v}\cdot\hat{\mathbf{n}}/c$ (see e.g. Cox & Gilliland 2003).

For each detector d in a dither we compute the effective pixel scale, s_d, as the mean pixel size given by the full astrometric solution, including the distortion terms. To remove the differences in scale between detectors, caused e.g. by the optical distortion, we consider the fractional change $\Delta s_d/s_d$ relative to the median of s_d over all dithers in all available fields. The scale change of a dither is the median of $\Delta s_d/s_d$ over the detectors, and the scale change, $\Delta s/s$, of a field is the median over its dithers. These values are then fitted as

$$\frac{\Delta s}{s} = k\,\frac{\mathbf{v}\cdot\hat{\mathbf{n}}}{c} + \text{const}\,, \quad (8)$$

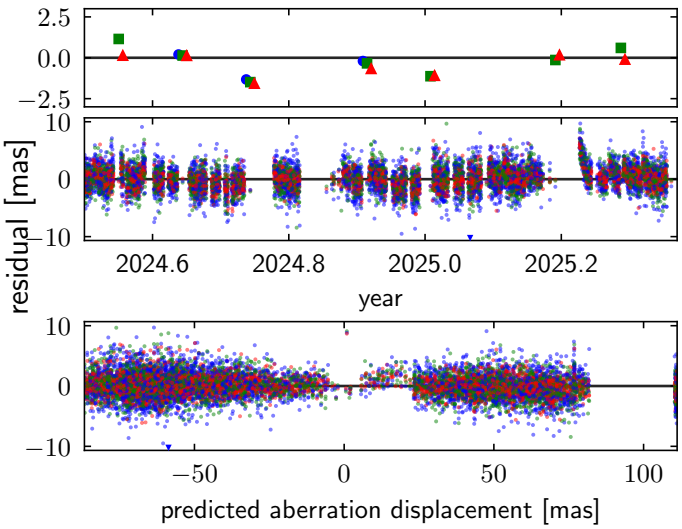


Fig. 8. Residuals between the measured and predicted aberration plate-scale change, expressed as the RMS displacement over the NISP field of view. Top: self-calibration visits as a function of time; error bars combine the error of the median over the dithers and the intrinsic visit-to-visit scatter. Middle: individual wide-survey fields as a function of time. Bottom: fields used in the fit as a function of the predicted aberration displacement. Symbols are coloured by band (Y_E: blue, J_E: green, H_E: red); triangles at the panel edges mark points beyond ±10 mas.

where $k = 1$ if the scale changes are reproduced by aberration, and the constant accounts for the arbitrary zero point. To express the results as displacements on the sky, we convert the fractional scale change into the RMS displacement it produces over the NISP field of view, $\delta = (\Delta s/s)\, r$, where $r = 18'$ is the RMS distance of the detector pixels from the centre of the field, computed from the astrometric solution. Likewise, the predicted displacement is $\delta_{\rm pred} = r\ (\mathbf{v}\cdot\hat{\mathbf{n}}/c)$,.

Figure 8 shows the residuals between the measured and predicted ($k = 1$ in Eq. 8) scale change, as a function of time and of the predicted displacement. We restrict the analysis to observations taken after July 2024, i.e. after the second thermal decontamination campaign (Euclid Collaboration: Schirmer et al. 2026), when *Euclid* had reached stable thermal conditions. In the self-calibration field, the displacement of stars due to aberration is close to its maximum, ∼ 20″, but it is a nearly uniform shift absorbed by the pointing. This field lies close to the North Ecliptic Pole, so the barycentric direction of its centre is almost perpendicular to the direction of motion of *Euclid* relative to the Solar System barycentre. The effect on the scale is therefore small, and corresponds to an absolute displacement of approximately 3 mas. Since the predicted displacement is small and the number of measurements lower, the constraint on k is correspondingly weaker, but still consistent with $k = 1$ within uncertainties. In the wide survey fields, instead, the predicted aberration displacement is within ±100 mas. The fit gives $k = 0.997 \pm 0.001$, consistent within the uncertainties in the three bands. The measured scale changes thus follow the expected aberration; after removing it, 68% of the fields deviate from the prediction by less than 2 mas, with no significant mean offset.

3.5. Parallax

As a further consistency check, we verify that the positions of stars in the self-calibration field observed at different epochs contain the parallax displacement expected for each star from *Gaia* DR3. Since the astrometric distortion is a smooth function of position on the detector, it can absorb a displacement common to all stars on a detector, but not the part that differs from star to star with their individual parallaxes. That part should remain fully in the calibrated positions, with the amplitude predicted from the *Gaia* DR3 parallax and the position of *Euclid* at each epoch. We test this with the observations of the self-calibration field, by measuring the parallax of individual stars from the calibrated positions alone and comparing it with *Gaia* DR3. The test is limited at faint magnitudes by the precision of the *Gaia* DR3 parallaxes and at bright magnitudes by saturation in NISP; since nearby red stars are brighter in the near-infrared than in the G band, the effect of these limits is to remove the reddest and nearest stars, and keep mostly red dwarfs with parallax $\varpi_{Gaia} \approx 2$–5 mas, and few with larger parallaxes. Moreover, the visits of the self-calibration field span about 1 year, too short to separate parallax from proper motion, which is therefore fixed to the *Gaia* DR3 value. Since the self-calibration dither pattern has large offsets, a star falls on the detectors in only a fraction of the 76 dithers in a visit, from about 60% near the centre of the pattern to a few per cent at its edge.

Positions in the calibrated NISP catalogs are matched (within 0.″3) to *Gaia* DR3 stars brighter than $G = 20$, `ruwe` < 1.4 and `astrometric_excess_noise` < 1 mas (Lindegren et al. 2021) that are not flagged as duplicated sources, and the residual $\boldsymbol{r} = (\Delta\alpha^*, \Delta\delta)$ with respect to the *Gaia* DR3 position propagated with proper motion only is computed at each exposure epoch. The barycentric position of *Euclid*, $\boldsymbol{b}$, is taken as the barycentric position of the Earth plus the geocentric position of the spacecraft given in the `POS_X/Y/Z` header keywords. With $\boldsymbol{b} = (X, Y, Z)$ expressed in au in ICRS axes, the parallax factors of a star at (α, δ) are, following the convention of the *Gaia* astrometric model,

$$\begin{aligned} F_{\alpha*} &= X\sin\alpha - Y\cos\alpha\,; \\ F_{\delta} &= X\sin\delta\cos\alpha + Y\sin\delta\sin\alpha - Z\cos\delta\,, \end{aligned} \tag{9}$$

so that a star of parallax ϖ is displaced by $\varpi\boldsymbol{F} = \varpi\,(F_{\alpha*}, F_\delta)$ in (α_*, δ).

Two sets of stars are used. *Probe* stars have a precise *Gaia* DR3 parallax ($\varpi > 2$ mas, $\varpi/\sigma_\varpi > 10$). *Anchor* stars are all other *Gaia* DR3 stars, regardless of their parallax. For each exposure and detector, the mean offset of the calibrated positions is computed from the anchors as $\boldsymbol{c} = \langle \boldsymbol{r} - \varpi_{Gaia}\boldsymbol{F}\rangle$ (with 4σ clipping), i.e. after removing the parallactic displacement of each anchor predicted from its own *Gaia* parallax. Without this subtraction, the mean anchor parallax (≈ a few tenths of a mas) would be absorbed by $\boldsymbol{c}$, biasing every probe parallax low by the same amount. The anchor-corrected probe offsets $\boldsymbol{y} = \boldsymbol{r} - \boldsymbol{c}$ and the parallax factors are then averaged over the dithers of each visit. For each probe with at least ten visits, $\varpi_{\rm NISP}$ is obtained by a least-squares fit of $\boldsymbol{y}_i = \varpi_{\rm NISP}\boldsymbol{F}_i + \boldsymbol{o}$ to its visit means, where the constant $\boldsymbol{o}$ absorbs the error of the propagated *Gaia* position, and its uncertainty $\sigma_{\rm NISP}$ from the scatter of the star's own residuals about the fit.

Due to the significant uncertainty in individual parallaxes, the comparison relies on the entire probe sample. We fit

$$\varpi_{\rm NISP} = k\,\varpi_{Gaia} + \delta \tag{10}$$

by least squares with weights $w_j = 1/(\sigma^2_{{\rm NISP},j} + \sigma^2_{\varpi,Gaia,j})$. A loss of part of the parallactic signal in the calibration would give $k < 1$, a zero-point offset would give $\delta \neq 0$. The difference between the NISP and *Gaia* DR3 parallaxes can be expressed

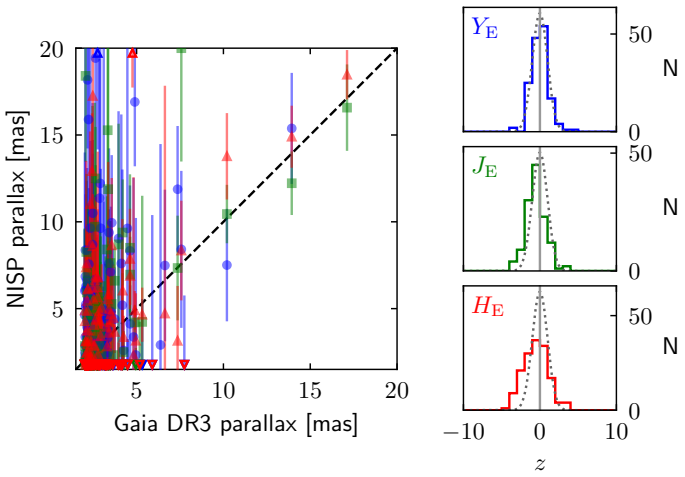


Fig. 9. Parallaxes of the probe stars measured from the calibrated NISP positions of the self-calibration field, versus their *Gaia* DR3 parallaxes. Left: Y_E (blue circles), J_E (green squares), and H_E (red triangles), for the stars with at least ten visits; error bars are the per-star uncertainties σ_{NISP}, derived from each star's own visit-to-visit scatter. Open triangles at the top and bottom edges mark NISP parallaxes outside the plotted range. The dashed line is the 1:1 relation. Right: distributions of the normalised differences z in Y_E, J_E, H_E (top to bottom), compared with a unit Gaussian scaled to the number of stars (dotted).

(Best et al. 2020) in units of their uncertainties, $z = (\varpi_{NISP} - \varpi_{Gaia})/(\sigma^2_{NISP} + \sigma^2_{\varpi,Gaia})^{1/2}$.

Figure 9 compares the NISP and *Gaia* DR3 parallaxes for 152, 126, and 157 probe stars in Y_E, J_E and H_E. In J_E and H_E we find $k = 1.03 \pm 0.11$ and 1.12 ± 0.16: the full parallactic amplitude is recovered. The same fits indicate a zero-point offset $\delta \approx -1$ mas in these bands (-0.92 ± 0.49 and -1.18 ± 0.52 mas), significant at about 2σ in each band. In Y_E, the most undersampled band and hence the one with the lowest astrometric precision, the constraints are weaker ($k = 0.73 \pm 0.29$, $\delta = +1.0 \pm 0.9$ mas) and consistent both with $k = 1$, $\delta = 0$ and with the J_E and H_E values. The median of z, with uncertainties bases on bootstrap resampling, is $+0.01 \pm 0.09$ (Y_E), -0.47 ± 0.12 (J_E), and -0.43 ± 0.18 (H_E), consistently with with the slight offset found above. The robust RMS is 1.07, 1.31, and 1.67 respectively. The negative medians in J and H reflect the zero-point offset discussed below.

We conclude that the NISP astrometric calibration preserves the stellar parallax: over the probe sample, the parallaxes recovered from the calibrated positions have an amplitude consistent with that of *Gaia* DR3, to 11–16% in J_E and H_E, the two bands that constrain it best, and at most $\approx 20\%$ of the signal could have been lost (2σ). The possible zero-point offset of ≈ -1 mas is marginal and well within the astrometric accuracy.

3.6. Inaccuracies due to persistence masking

As anticipated in Sect. 3.1, the validation of the DR1 data products indicated that, for a specific number of dithers, the residuals in certain detectors, particularly DET13 and DET14, are higher than those in other detectors, exceeding 100 mas. A comprehensive analysis revealed that, in these instances, the flagging of pixels is affected by persistence. Persistence can cause false detections, and as detailed in Euclid Collaboration: Polenta et al. (2026a), pixels in the persistence image that exceed a threshold of $2\,e^-$ are considered invalid in the NISP images. However, this choice leads to a notable decrease in the number of sources with matches in the *Gaia* DR3 catalogue, reducing from approximately 30 per detector to just a few, which in turn results in less accurate astrometric calibration. Shortly after this issue was identified, a solution was implemented (Sect. 4.1); however, it could not be incorporated into DR1.

To better estimate the impact of these failures on DR1, the following analysis has been conducted. For each stacked catalogue generated in DR1 for a specific `OBSID`, detected sources are matched to the *Gaia* DR3 catalogue within a 5″ radius to account for catastrophic astrometric failures. A similar procedure is employed to compare the NISP and VIS positions. In this case, VIS sources are initially selected with `|spread_model|` < 0.05 in the stacked VIS catalogues (Euclid Collaboration: McCracken et al. 2026) to exclude overly extended sources.

An RMS map is subsequently constructed utilising a 2D rolling window approach. The area covered by each stacked catalogue is divided into a grid with 30″ intervals: this step size is chosen to achieve a finer spatial resolution and more detailed data sampling across the observed area. At the centre of each grid cell, matched sources are gathered within a specified radius, selected to ensure that each cell contains at least 10 (20) matched *Gaia* DR3 (VIS) sources. This results in a radius of 4′ for *Gaia* DR3 and 2′ for VIS; in the latter case, the radius is smaller because aligning with the VIS catalogue increases the number of matches with fainter NISP sources. If a cell contains fewer than the minimum required matches, the radius is incrementally increased by 10″ until the requirement is met. On average, each cell contains 30, 50 matches with *Gaia* DR3 and VIS respectively.

This approach enables us to identify regions where the RMS surpasses a predetermined threshold without significantly increasing the computational time. For each `OBSID`, a specific RMS map is generated. assigning the highest RMS values observed across the NISP bands to each element of the map. The results of the comparison with VIS and *Gaia* DR3 (Fig. 10) are consistent: the RMS exceeds 30, 60, and 90 mas in 3%, 0.3%, and 0.1% respectively of the total area, with a median RMS of approximately 20 mas. Finally, the same procedure is repeated using H_E as a reference and measuring the RMS in J_E and Y_E. This produces results similar to those obtained previously, with RMS exceeding 30, 60, and 90 mas in 1%, 0.2%, and 0.1% respectively of the area for each of J_E and Y_E compared to H_E.

These tests indicate that despite this issue related to persistence masking, which will be resolved in Data Release 2 (Sect. 4.1), the astrometry remains consistent when compared to VIS and across the three NISP channels. The RMS is less than 30 mas (0.1 pixels) for at least 97% of the surveyed area when comparing VIS to NISP. Across the NISP bands, the RMS is less than 30 mas (0.1 pixels) for 99% of the area.

4. Improvements for DR2 and beyond

4.1. Reducing the impact on astrometry of the persistence masking

Although it was not feasible to rectify the persistence issue in DR1, a solution has been developed and applied to subsequent processing. Astrometric calibration can be influenced by persistence, either through false detections that result in spurious matches or by false detections near real sources that disrupt the centroid estimate. The impact of persistence flagging can be mitigated if a detection is discarded only when the pixels within a defined radius R_p from the detection centre exceed a specified persistence threshold I_p. This ensures that only genuinely spurious detections are rejected, or those detections whose centre

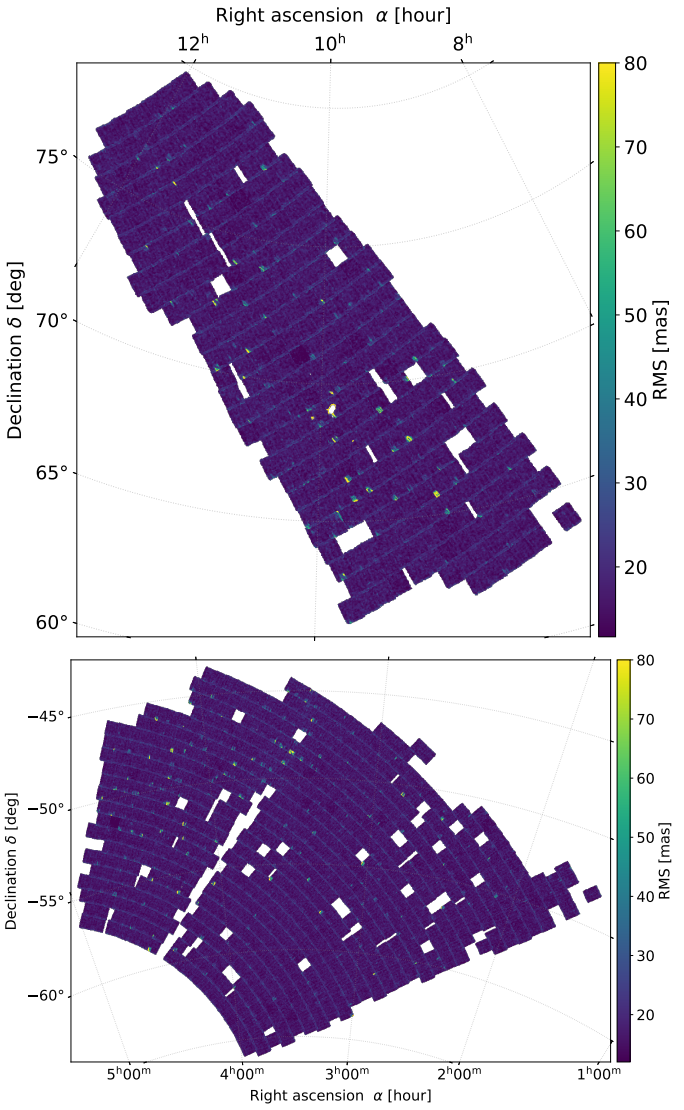


Fig. 10. RMS maps derived from the spatial analysis of the Y_E, J_E, andH_E detections compared to VIS. The small green/yellow spots indicate areas where persistence flagging has led to reduced astrometric accuracy.

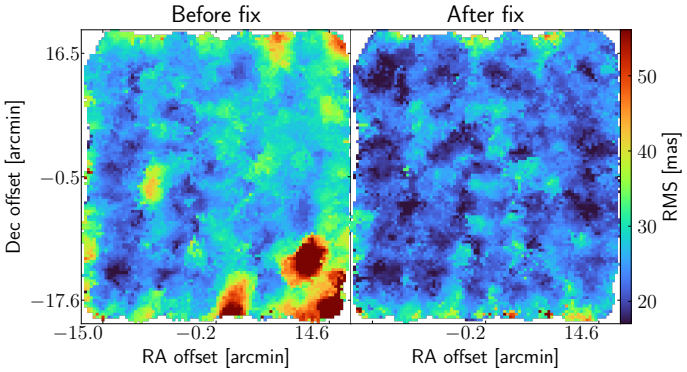


Fig. 11. RMS maps derived for a single observation ID both before and after applying the fix to mitigate the effects of persistence flagging. Initially, this led to a region with RMS > 60 mas (left), which vanished after the fix was implemented (right).

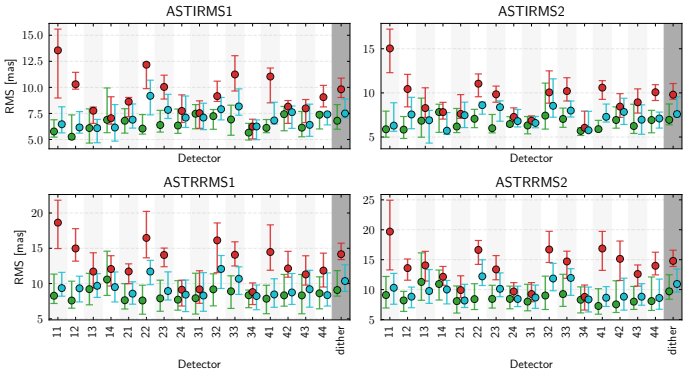


Fig. 12. RMS residuals calculated for a subset of 10 observations (40 dithers), both for individual detectors and across the entire dither. The colours illustrate RMS values, including the median and 25%/75% percentiles, derived from various methods across detectors: green represents a comprehensive polynomial fit (current pipeline); red indicates a scenario with constant distortion where only linear terms are fitted; and cyan reflects constant distortion followed by a second-order fit. The RMS over the dithers is shown at the end and is highlighted in grey.

estimates may be compromised by persistence features. The values of I_p and R_p are determined following an analysis conducted on a subset of dithers: $I_p = 5e^-$ (see also Euclid Collaboration: Kubik et al. 2026) and $R_p = 5$ pixels. Figure 11 demonstrates the impact of the fix on the astrometric residuals on a single observation ID.

4.2. Exploring a simplified distortion model: preliminary Investigation

In DR1, the presolution is merely utilised in `Scamp` to enhance the initial matching of detected and *Gaia* DR3 sources. As discussed in Sect. 3.3, the distortion appears to be stable enough to consider keeping it constant while fitting only the linear terms.

This alternative approach involves directly applying the presolution distortion model, assumed to be constant, to the source positions, followed by the computation of only the linear terms that are specific to each dither. This simplified model would reduce computational complexity and minimise the sensitivity of the astrometric calibration to noise or spurious variations, potentially mitigating the risk of overfitting.

The underlying assumption here is that the linear corrections capture the residual variations due to the NISP optics (Sect. 2). To initially evaluate the validity of this assumption, we developed a modified version of `NIR_Astrometry` employing an approach similar to that outlined in Sect. 3.3, and conducted a pilot study based on a limited set of 10 observations (40 dithers): initially, the presolution is converted into the `SIP` formalism, which is then employed to remove distortion from the pixel coordinates in the `SExtractor` catalogue. `Scamp` is subsequently executed on this modified catalogue. Two options are considered: (1) no additional distortion is computed in this second step, with only the linear terms being refitted, and (2) a polynomial of order 2 is fitted. Figure 12, which illustrates the RMS of the residuals, supports the conclusions presented in Sect. 3.3: relying solely on linear terms results in an increased RMS of the residuals. To achieve RMS values comparable to those obtained with the full fitting (10 mas), it is necessary to incorporate an additional second-order component. A simplified distortion model with fewer free parameters would still allow for a reduction in the computational complexity; however, further comprehensive testing across a larger dataset is required before considering potential integration into the pipeline.

5. Conclusions

This paper has presented the methodology and results of the astrometric calibration applied to the NISP data in Euclid DR1. The calibration pipeline employs the `Scamp` software to model and correct instrumental distortions on a per-dither basis, using a polynomial distortion representation within the `PV` formalism. The *Gaia* DR3 catalogue serves as the external astrometric reference, with source selections and quality controls implemented to ensure robust matching and calibration accuracy.

Analysis of 4000 observations covering 1950 deg^2 and over 1 year of observations demonstrates that the NIR astrometric calibration achieves an average precision of approximately 10 mas, with 99% of the dithers exhibiting residuals below 20 mas in each detector. This corresponds to less than 0.1 pixels, and is within the requirement of 30 mas. The average offsets relative to *Gaia* DR3 are negligible (within 2 mas), confirming the absence of significant systematic biases.

The analysis of the stacked catalogues confirms these values, allowing further tests. Spatial mapping of the residuals across the focal plane shows stable performance, with minor variations at the edges attributed to the dithering patterns. The astrometric consistency among the neighbouring dithers is confirmed by matching sources in overlapping areas across the stacks. The chromaticity effects on astrometry are minimal, with slopes below 1 mas mag^{-1}, and no significant temporal or telescope rotation dependencies is observed. The distortion pattern is stable over time within approximately 10 mas, supporting the potential for a constant distortion model supplemented by an additional correction to capture the residual variations. However, tests indicate that fitting only linear terms increases the residuals, and a second-order polynomial fit is necessary to maintain a calibration accuracy comparable to that of the full polynomial model.

A limitation identified in DR1 is the impact of persistence masking on astrometric accuracy, particularly affecting detectors DET13 and DET14. Excessive flagging of pixels due to persistence reduces the number of matched sources and may locally degrade the calibration precision. Upon comparison with the VIS detections, it is found that this issue (RMS $>$ 30 mas) impacts less than 5% of the surveyed area. This test also allows us to verify the astrometric consistency across the different NISP bands. A mitigation strategy involving a refined persistence flagging criterion based on persistence intensity and radius around detections has been developed and applied in subsequent processing, effectively restoring astrometric accuracy in the affected regions.

For future data releases, improvements include a refined persistence masking approach and exploration of alternative distortion evaluation methods that reduce the complexity of the distortion model while preserving the calibration quality. These enhancements aim to increase the calibration robustness and computational efficiency.

In conclusion, the *Euclid* NISP astrometric calibration in DR1 demonstrates high precision and stability, with well-characterised residuals and identified pathways for further improvement. The results provide a solid foundation for subsequent data releases, ensuring accurate celestial source positioning, which is essential for the mission's scientific objectives.

Acknowledgements. The Euclid Consortium acknowledges the European Space Agency and a number of agencies and institutes that have supported the development of *Euclid*, in particular the Agenzia Spaziale Italiana, the Austrian Forschungsförderungsgesellschaft funded through BMIMI, the Belgian Science Policy, the Canadian Euclid Consortium, the Deutsches Zentrum für Luft- und Raumfahrt, the DTU Space and the Niels Bohr Institute in Denmark, the French Centre National d'Etudes Spatiales, the Fundação para a Ciência e a Tecnologia, the Hungarian Academy of Sciences, the Ministerio de Ciencia, Innovación y Universidades, the National Aeronautics and Space Administration, the National Astronomical Observatory of Japan, the Netherlandse Onderzoekschool Voor Astronomie, the Norwegian Space Agency, the Research Council of Finland, the Romanian Space Agency, the Swiss Space Office (SSO) at the State Secretariat for Education, Research, and Innovation (SERI), and the United Kingdom Space Agency. A complete and detailed list is available on the *Euclid* web site (www.euclid-ec.org/consortium/community/). This work has made use of the Euclid Data Release 1 (DR1) from the European Space Agency (ESA) mission *Euclid*, available at https://www.cosmos.esa.int/web/euclid/data-release-dr1. This research makes use of ESA Datalabs (datalabs.esa.int), an initiative by ESA's Data Science and Archives Division in the Science and Operations Department, Directorate of Science. This work has made use of data from the European Space Agency (ESA) mission *Gaia* (https://www.cosmos.esa.int/gaia), processed by the *Gaia* Data Processing and Analysis Consortium (DPAC, https://www.cosmos.esa.int/web/gaia/dpac/consortium). Funding for the DPAC has been provided by national institutions, in particular the institutions participating in the *Gaia* Multilateral Agreement.

References

Bertin, E. 2006, in ASP Conference Series, Vol. 351, Astronomical Data Analysis Software and Systems XV, ed. C. Gabriel, C. Arviset, D. Ponz, & S. Enrique, 112
Bertin, E. 2011, in Astronomical Society of the Pacific Conference Series, Vol. 442, Astronomical Data Analysis Software and Systems XX, ed. I. N. Evans, A. Accomazzi, D. J. Mink, & A. H. Rots, 435
Bertin, E. & Arnouts, S. 1996, A&AS, 117, 393
Best, W. M. J., Liu, M. C., Magnier, E. A., & Dupuy, T. J. 2020, AJ, 159, 257
Calabretta, M. R. & Greisen, E. W. 2002, A&A, 395, 1077
Cox, C. & Gilliland, R. L. 2003, in HST Calibration Workshop : Hubble after the Installation of the ACS and the NICMOS Cooling System, ed. S. Arribas, A. Koekemoer, & B. Whitmore, 58
Euclid Collaboration: da Silva, R., Faustini, F., Polenta, G., et al. 2026, A&A, submitted
Euclid Collaboration: Jahnke, K., Gillard, W., Schirmer, M., et al. 2025, A&A, 697, A3
Euclid Collaboration: Kubik, B., Conseil, S., Ferriol, S., et al. 2026, A&A, submitted
Euclid Collaboration: McCracken, H. J., Benson, K., Dolding, C., et al. 2026, A&A, 711, A2
Euclid Collaboration: Mellier, Y., Abdurro'uf, Acevedo Barroso, J., et al. 2025, A&A, 697, A1
Euclid Collaboration: Polenta, G., Frailis, M., Alavi, A., et al. 2026a, A&A, submitted
Euclid Collaboration: Polenta, G., Frailis, M., Alavi, A., et al. 2026b, A&A, 711, A3
Euclid Collaboration: Scaramella, R., Amiaux, J., Mellier, Y., et al. 2022, A&A, 662, A112
Euclid Collaboration: Schirmer, M., Jahnke, K., Seidel, G., et al. 2022, A&A, 662, A92
Euclid Collaboration: Schirmer, M., Paterson, K., Altieri, B., et al. 2026, A&A, submitted
Euclid Data Release 1. 2026, https://doi.org/10.57780/esa-d079c51
Gaia Collaboration: Prusti, T., de Bruijne, J. H. J., Brown, A. G. A., et al. 2016, A&A, 595, A1
Gaia Collaboration: Vallenari, A., Brown, A. G. A., Prusti, T., et al. 2023, A&A, 674, A1
Lindegren, L., Klioner, S. A., Hernández, J., et al. 2021, A&A, 649, A2
Shupe, D. L., Laher, R. R., Storrie-Lombardi, L., et al. 2012, in SPIE Conference Series, Vol. 8451, Software and Cyberinfrastructure for Astronomy II, ed. N. M. Radziwill & G. Chiozzi, 84511M
Shupe, D. L., Moshir, M., Li, J., et al. 2005, in ASP Conference Series, Vol. 347, Astronomical Data Analysis Software and Systems XIV, ed. P. Shopbell, M. Britton, & R. Ebert, 491
Vallenari, A. 2022, in EAS2022, European Astronomical Society Annual Meeting, 2358

Authors and affiliations

Euclid Collaboration: M. Radovich[⋆1], R. da Silva[2,3], G. Polenta[3], A. Alavi[4], H. Aussel[5], P. Awad[6], A. Bonchi[3], L. Bramante[7], S. Conseil[8,9], M. Correnti[2,3], L. V. Costa[7], I. Das[4], F. Faustini[2], M. Frailis[10], Y. Fu[6,11], T. Gasparetto[2], W. Gillard[12], S. Hemmati[4], J. Jacobson[4], K. Jahnke[13], B. Kubik[9], C. Macabiau[9], P. W. Morris[14], K. Paterson[13], M. Schirmer[13], H. I. Teplitz[15], A. Troja[10], B. Altieri[16], S. Andreon[17], N. Auricchio[18], C. Baccigalupi[19,10,20,21], M. Baldi[22,18,23], A. Balestra[1], P. Battaglia[18], A. N. Belikov[11,24], A. Biviano[10,19], M. Bolzonella[18], E. Branchini[25,26,17], M. Brescia[27,28], J. Brinchmann[29,30,31], S. Camera[32,33,34], G. Cañas-Herrera[6], V. Capobianco[34], C. Carbone[35], J. Carretero[36,37], M. Castellano[2], G. Castignani[18], S. Cavuoti[28,38], A. Cimatti[39], C. Colodro-Conde[40], G. Congedo[41], C. J. Conselice[42], L. Conversi[43,16], Y. Copin[9], A. Costille[44], H. M. Courtois[45], A. Da Silva[46,47], H. Degaudenzi[48], G. De Lucia[10], H. Dole[49,50], F. Dubath[48], C. A. J. Duncan[41], X. Dupac[16], S. Dusini[51], S. Escoffier[12], M. Farina[52], S. Farrens[5], S. Ferriol[9], F. Finelli[18,53], S. Fotopoulou[54], N. Fourmanoit[12], E. Franceschi[18], M. Fumana[35], L. Gabarra[55], S. Galeotta[10], K. George[56], B. Gillis[41], C. Giocoli[18,23], J. Gracia-Carpio[57], A. Grazian[1], F. Grupp[57,58], L. Guzzo[59,17,60], W. G. Hartley[48], S. V. H. Haugan[61], H. Hoekstra[6], W. Holmes[62], I. M. Hook[63], F. Hormuth[64], A. Hornstrup[65,66], M. Jhabvala[67], S. Kermiche[12], A. Kiessling[62], R. Kohley[16], M. Kümmel[58], M. Kunz[68], H. Kurki-Suonio[69,70], A. M. C. Le Brun[71], D. Le Mignant[44], S. Ligori[34], P. B. Lilje[61], V. Lindholm[69,70], I. Lloro[72], M. Magliocchetti[52], G. Mainetti[73], O. Mansutti[10], S. Marcin[74], O. Marggraf[75], M. Martinelli[2,76], N. Martinet[44], F. Marulli[77,18,23], R. J. Massey[78], N. Mauri[39,23], H. J. McCracken[79], C. J. R. McPartland[66,80], E. Medinaceli[18], S. Mei[81,82], M. Melchior[83], M. Meneghetti[18,23], E. Merlin[1], G. Meylan[84], P. Monaco[85,10,20,19], A. Mora[86], M. Moresco[77,18], C. Moretti[10,19,20], L. Moscardini[77,18,23], R. Nakajima[75], C. Neissner[87,37], R. C. Nichol[88], S.-M. Niemi[89], C. Padilla[87], S. Paltani[48], F. Pasian[10], W. J. Percival[90,91,92], V. Pettorino[89], A. Pezzotta[17], M. Poncet[93], L. A. Popa[94], F. Raison[57], A. Refregier[95], A. Renzi[96,51,18], J. Rhodes[62], G. Riccio[28], I. Risso[25,26,17], H.-W. Rix[13], F. Rizzo[10], E. Romelli[10], C. Rosset[81], B. Rusholme[4], R. Saglia[58,57], Z. Sakr[97,98,99], A. G. Sánchez[57], D. Sapone[100], B. Sartoris[101], P. Schneider[75], A. Secroun[12], E. Sihvola[69,70], C. Sirignano[96,51], G. Sirri[23], L. Stanco[51], P. Tallada-Crespí[36,37], A. N. Taylor[41], I. Tereno[46,47], N. Tessore[102], S. Toft[103,80], R. Toledo-Moreo[104,105], F. Torradeflot[37,36], A. Tsyganov[106], I. Tutusaus[107,108,98], J. Valiviita[69,70], T. Vassallo[10,56], A. Veropalumbo[17,26,25], Y. Wang[4], J. Weller[58,57], A. Zacchei[10,19], G. Zamorani[18], F. M. Zerbi[17], E. Zucca[18], I. T. Andika[58], M. Ballardini[109,110,18], P. Bergamini[18], S. Borgani[85,19,10,20,111], E. Bozzo[48], C. Burigana[112,53], R. Cabanac[98], M. Calabrese[113,35], A. Cappi[101,18], F. Caro[2], T. Castro[114,10,19], D. Di Ferdinando[23], J. A. Escartin Vigo[57], G. Fabbian[49], J. García-Bellido[97], C. M. Gutierrez[40,115], A. Hall[41], Y. Kang[116], A. Loureiro[117,118], J. Macias-Perez[119], R. Maoli[120,2], R. B. Metcalf[77,18], M. Pöntinen[69], E. Sarpa[10], V. Scottez[121,122], M. Sereno[18,23], K. Tanidis[123], M. Tenti[23], M. Tucci[48], M. Viel[19,10,21,20,111], M. Wiesmann[61], J. A. Acevedo Barroso[62], Y. Akrami[97,124], G. Angora[28,109], S. Anselmi[51,96,125], M. Archidiacono[59,60], G. Aricò[23], F. Atrio-Barandela[126], M. Aubert[9], M. Baes[127], L. Bazzanini[109,18], J. R. Bermejo-Climent[128,129], D. Bertacca[96,1,51], M. Bethermin[130], F. Beutler[41], A. Blanchard[98], F. Bouchè[131,38], M. L. Brown[42], S. Bruton[14], A. Calabro[2], B. Camacho Quevedo[19,21,10], P. Carrilho[132], C. S. Carvalho[133], Y. Charles[44], F. Cogato[18], T. E. Collett[134], A. R. Cooray[135], P. Corcho-Caballero[11], B. Csizi[116], O. Cucciati[18], T. de Boer[136], G. Desprez[11], A. Díaz-Sánchez[137], S. Di Domizio[25,26], J. M. Diego[138], V. Duret[12], A. Enia[139,18], Y. Fang[58], A. Farina[17,26], A. M. N. Ferguson[41], A. Finoguenov[69], A. Franco[140,141,142], A. Fumagalli[10], K. Ganga[81], R. Gavazzi[44,79], E. Gaztanaga[107,108,134], Z. Ghaffari[10,19], F. Giacomini[23], F. Gianotti[18], G. Gozaliasl[143,69], A. Gruppuso[18,23], M. Guidi[22,18], C. Hernández-Monteagudo[115,40], T. Heuberger[74], H. Hildebrandt[144], J. Hjorth[145], M. Jauzac[146,78,147,148,98], J. J. E. Kajava[149,150,151], V. Kansal[152,153], J. Kim[55], C. C. Kirkpatrick[154], A. Kovács[129,128], I. Kovačić[127], K. Koyama[134], S. Kruk[16], M. C. Lam[41], M. Lattanzi[110], S. Lee[155,62], L. Legrand[156,49], M. D. Lepinzan[10], G. Leroy[146,78], J. Lesgourgues[157], T. I. Liaudat[158], L. Linke[116], S. J. Liu[52], G. Maggio[10], F. Mannucci[159], F. R. Marleau[116], C. J. A. P. Martins[160,29], M. Miluzio[16,161], G. Morgante[18], S. Nadathur[134], K. Naidoo[134,13], P. Natoli[109,110], A. Navarro-Alsina[75], S. Nesseris[97], F. Oppizzi[26,51,96], F. Pace[32,33,34,47], D. Paoletti[18,53], F. Passalacqua[51], L. Patrizii[23], C. Pattison[134], A. Pisani[12], L. Pizzuti[162], D. Potter[163], M. Poulain[164], G. W. Pratt[5], S. Quai[77,18], G. Rodighiero[96,1], W. Roster[57], M. Sahlén[165], D. B. Sanders[136], A. Schneider[163], M. Schultheis[101], D. Sciotti[2,76], E. Sellentin[166,6], S. Serjeant[167], L. C. Smith[168], J. G. Sorce[169,49], I. Szapudi[136], M. Talia[77,18], F. Tarsitano[170,95], G. Testera[26], R. Teyssier[171], S. Tosi[25,17,26], C. Uhlemann[172,173], C. Valieri[23], A. Venhola[164], D. Vergani[18], P. Vielzeuf[12], E. Vilenius[102], S. Vinciguerra[44], M. von Wietersheim-Kramsta[78,146], N. A. Walton[168], A. H. Wright[144], and D. Scott[174]

[1] INAF-Osservatorio Astronomico di Padova, Via dell'Osservatorio 5, 35122 Padova, Italy
[2] INAF-Osservatorio Astronomico di Roma, Via Frascati 33, 00078 Monteporzio Catone, Italy

[3] Space Science Data Center, Italian Space Agency, via del Politecnico snc, 00133 Roma, Italy
[4] Caltech/IPAC, 1200 E. California Blvd., Pasadena, CA 91125, USA
[5] Université Paris-Saclay, Université Paris Cité, CEA, CNRS, AIM, 91191, Gif-sur-Yvette, France
[6] Leiden Observatory, Leiden University, Einsteinweg 55, 2333 CC Leiden, The Netherlands
[7] Aerospace Logistics Technology Engineering Company, Corso Marche 79, 10146 Torino, Italy
[8] Centre de Recherche Astrophysique de Lyon, UMR5574, CNRS, Université Claude Bernard Lyon 1, ENS de Lyon, 69230, Saint-Genis-Laval, France
[9] Université Lyon 1, CNRS/IN2P3, IP2I Lyon, Villeurbanne, France
[10] INAF-Osservatorio Astronomico di Trieste, Via G. B. Tiepolo 11, 34143 Trieste, Italy
[11] Kapteyn Astronomical Institute, University of Groningen, PO Box 800, 9700 AV Groningen, The Netherlands
[12] Aix-Marseille Université, CNRS/IN2P3, CPPM, Marseille, France
[13] Max-Planck-Institut für Astronomie, Königstuhl 17, 69117 Heidelberg, Germany
[14] California Institute of Technology, 1200 E California Blvd, Pasadena, CA 91125, USA
[15] Infrared Processing and Analysis Center, California Institute of Technology, Pasadena, CA 91125, USA
[16] ESAC/ESA, Camino Bajo del Castillo, s/n., Urb. Villafranca del Castillo, 28692 Villanueva de la Cañada, Madrid, Spain
[17] INAF-Osservatorio Astronomico di Brera, Via Brera 28, 20122 Milano, Italy
[18] INAF-Osservatorio di Astrofisica e Scienza dello Spazio di Bologna, Via Piero Gobetti 93/3, 40129 Bologna, Italy
[19] IFPU, Institute for Fundamental Physics of the Universe, via Beirut 2, 34151 Trieste, Italy
[20] INFN, Sezione di Trieste, Via Valerio 2, 34127 Trieste TS, Italy
[21] SISSA, International School for Advanced Studies, Via Bonomea 265, 34136 Trieste TS, Italy
[22] Dipartimento di Fisica e Astronomia, Università di Bologna, Via Gobetti 93/2, 40129 Bologna, Italy
[23] INFN-Sezione di Bologna, Viale Berti Pichat 6/2, 40127 Bologna, Italy
[24] ATG Europe BV, Huygensstraat 34, 2201 DK Noordwijk, The Netherlands
[25] Dipartimento di Fisica, Università di Genova, Via Dodecaneso 33, 16146, Genova, Italy
[26] INFN-Sezione di Genova, Via Dodecaneso 33, 16146, Genova, Italy
[27] Department of Physics "E. Pancini", University Federico II, Via Cinthia 6, 80126, Napoli, Italy
[28] INAF-Osservatorio Astronomico di Capodimonte, Via Moiariello 16, 80131 Napoli, Italy
[29] Instituto de Astrofísica e Ciências do Espaço, Universidade do Porto, CAUP, Rua das Estrelas, PT4150-762 Porto, Portugal
[30] Faculdade de Ciências da Universidade do Porto, Rua do Campo de Alegre, 4150-007 Porto, Portugal
[31] European Southern Observatory, Karl-Schwarzschild-Str. 2, 85748 Garching, Germany
[32] Dipartimento di Fisica, Università degli Studi di Torino, Via P. Giuria 1, 10125 Torino, Italy
[33] INFN-Sezione di Torino, Via P. Giuria 1, 10125 Torino, Italy
[34] INAF-Osservatorio Astrofisico di Torino, Via Osservatorio 20, 10025 Pino Torinese (TO), Italy
[35] INAF-IASF Milano, Via Alfonso Corti 12, 20133 Milano, Italy
[36] Centro de Investigaciones Energéticas, Medioambientales y Tecnológicas (CIEMAT), Avenida Complutense 40, 28040 Madrid, Spain
[37] Port d'Informació Científica, Campus UAB, C. Albareda s/n, 08193 Bellaterra (Barcelona), Spain
[38] INFN – Sezione di Napoli, Via Cinthia 6, 80126, Napoli, Italy
[39] Dipartimento di Fisica e Astronomia "Augusto Righi" - Alma Mater Studiorum Università di Bologna, Viale Berti Pichat 6/2, 40127 Bologna, Italy
[40] Instituto de Astrofísica de Canarias, E-38205 La Laguna, Tenerife, Spain
[41] Institute for Astronomy, University of Edinburgh, Royal Observatory, Blackford Hill, Edinburgh EH9 3HJ, UK
[42] Jodrell Bank Centre for Astrophysics, Department of Physics and Astronomy, University of Manchester, Oxford Road, Manchester M13 9PL, UK
[43] European Space Agency/ESRIN, Largo Galileo Galilei 1, 00044 Frascati, Roma, Italy
[44] Aix-Marseille Université, CNRS, CNES, LAM, Marseille, France
[45] Université Lyon 1, CNRS/IN2P3, IUF, IP2I Lyon, Villeurbanne, France
[46] Departamento de Física, Faculdade de Ciências, Universidade de Lisboa, Edifício C8, Campo Grande, PT1749-016 Lisboa, Portugal
[47] Instituto de Astrofísica e Ciências do Espaço, Faculdade de Ciências, Universidade de Lisboa, Campo Grande, 1749-016 Lisboa, Portugal
[48] Department of Astronomy, University of Geneva, ch. d'Ecogia 16, 1290 Versoix, Switzerland
[49] Université Paris-Saclay, CNRS, Institut d'astrophysique spatiale, 91405, Orsay, France
[50] Institut universitaire de France (IUF), 1 rue Descartes, 75231 PARIS CEDEX 05, France
[51] INFN-Padova, Via Marzolo 8, 35131 Padova, Italy
[52] INAF-Istituto di Astrofisica e Planetologia Spaziali, via del Fosso del Cavaliere, 100, 00100 Roma, Italy
[53] INFN-Bologna, Via Irnerio 46, 40126 Bologna, Italy
[54] School of Physics, HH Wills Physics Laboratory, University of Bristol, Tyndall Avenue, Bristol, BS8 1TL, UK
[55] Department of Physics, University of Oxford, Keble Road, Oxford OX1 3RH, UK
[56] University Observatory, LMU Faculty of Physics, Scheinerstr. 1, 81679 Munich, Germany
[57] Max Planck Institute for Extraterrestrial Physics, Giessenbachstr. 1, 85748 Garching, Germany
[58] Universitäts-Sternwarte München, Fakultät für Physik, Ludwig-Maximilians-Universität München, Scheinerstr. 1, 81679 München, Germany
[59] Dipartimento di Fisica "Aldo Pontremoli", Università degli Studi di Milano, Via Celoria 16, 20133 Milano, Italy
[60] INFN-Sezione di Milano, Via Celoria 16, 20133 Milano, Italy
[61] Institute of Theoretical Astrophysics, University of Oslo, P.O. Box 1029 Blindern, 0315 Oslo, Norway
[62] Jet Propulsion Laboratory, California Institute of Technology, 4800 Oak Grove Drive, Pasadena, CA, 91109, USA
[63] School of Physics and Astronomy, Lancaster University, Lancaster, LA1 4YB, UK
[64] Felix Hormuth Engineering, Goethestr. 17, 69181 Leimen, Germany
[65] Technical University of Denmark, Elektrovej 327, 2800 Kgs. Lyngby, Denmark
[66] Cosmic Dawn Center (DAWN), Denmark
[67] NASA Goddard Space Flight Center, Greenbelt, MD 20771, USA
[68] Université de Genève, Département de Physique Théorique and Centre for Astroparticle Physics, 24 quai Ernest-Ansermet, CH-1211 Genève 4, Switzerland

[69] Department of Physics, P.O. Box 64, University of Helsinki, 00014 Helsinki, Finland
[70] Helsinki Institute of Physics, Gustaf Hällströmin katu 2, University of Helsinki, 00014 Helsinki, Finland
[71] Laboratoire d'etude de l'Univers et des phenomenes eXtremes, Observatoire de Paris, Université PSL, Sorbonne Université, CNRS, 92190 Meudon, France
[72] SKAO, Jodrell Bank, Lower Withington, Macclesfield SK11 9FT, UK
[73] Centre de Calcul de l'IN2P3/CNRS, 21 avenue Pierre de Coubertin 69627 Villeurbanne Cedex, France
[74] University of Applied Sciences and Arts of Northwestern Switzerland, School of Computer Science, 5210 Windisch, Switzerland
[75] Universität Bonn, Argelander-Institut für Astronomie, Auf dem Hügel 71, 53121 Bonn, Germany
[76] INFN-Sezione di Roma, Piazzale Aldo Moro, 2 - c/o Dipartimento di Fisica, Edificio G. Marconi, 00185 Roma, Italy
[77] Dipartimento di Fisica e Astronomia "Augusto Righi" - Alma Mater Studiorum Università di Bologna, via Piero Gobetti 93/2, 40129 Bologna, Italy
[78] Department of Physics, Institute for Computational Cosmology, Durham University, South Road, Durham, DH1 3LE, UK
[79] Institut d'Astrophysique de Paris, UMR 7095, CNRS, and Sorbonne Université, 98 bis boulevard Arago, 75014 Paris, France
[80] Niels Bohr Institute, University of Copenhagen, Jagtvej 128, 2200 Copenhagen, Denmark
[81] Université Paris Cité, CNRS, Astroparticule et Cosmologie, 75013 Paris, France
[82] CNRS-UCB International Research Laboratory, Centre Pierre Binétruy, IRL2007, CPB-IN2P3, Berkeley, USA
[83] University of Applied Sciences and Arts of Northwestern Switzerland, School of Engineering, 5210 Windisch, Switzerland
[84] Institute of Physics, Laboratory of Astrophysics, Ecole Polytechnique Fédérale de Lausanne (EPFL), Observatoire de Sauverny, 1290 Versoix, Switzerland
[85] Dipartimento di Fisica - Sezione di Astronomia, Università di Trieste, Via Tiepolo 11, 34131 Trieste, Italy
[86] Telespazio UK S.L. for European Space Agency (ESA), Camino bajo del Castillo, s/n, Urbanizacion Villafranca del Castillo, Villanueva de la Cañada, 28692 Madrid, Spain
[87] Institut de Física d'Altes Energies (IFAE), The Barcelona Institute of Science and Technology, Campus UAB, 08193 Bellaterra (Barcelona), Spain
[88] School of Mathematics and Physics, University of Surrey, Guildford, Surrey, GU2 7XH, UK
[89] European Space Agency/ESTEC, Keplerlaan 1, 2201 AZ Noordwijk, The Netherlands
[90] Waterloo Centre for Astrophysics, University of Waterloo, Waterloo, Ontario N2L 3G1, Canada
[91] Department of Physics and Astronomy, University of Waterloo, Waterloo, Ontario N2L 3G1, Canada
[92] Perimeter Institute for Theoretical Physics, Waterloo, Ontario N2L 2Y5, Canada
[93] Centre National d'Etudes Spatiales – Centre spatial de Toulouse, 18 avenue Edouard Belin, 31401 Toulouse Cedex 9, France
[94] Institute of Space Science, Str. Atomistilor, nr. 409 Măgurele, Ilfov, 077125, Romania
[95] Institute for Particle Physics and Astrophysics, Dept. of Physics, ETH Zurich, Wolfgang-Pauli-Strasse 27, 8093 Zurich, Switzerland
[96] Dipartimento di Fisica e Astronomia "G. Galilei", Università di Padova, Via Marzolo 8, 35131 Padova, Italy
[97] Instituto de Física Teórica UAM-CSIC, Campus de Cantoblanco, 28049 Madrid, Spain
[98] Institut de Recherche en Astrophysique et Planétologie (IRAP), Université de Toulouse, CNRS, UPS, CNES, 14 Av. Edouard Belin, 31400 Toulouse, France
[99] Université St Joseph; Faculty of Sciences, Beirut, Lebanon
[100] Departamento de Física, FCFM, Universidad de Chile, Blanco Encalada 2008, Santiago, Chile
[101] Université Côte d'Azur, Observatoire de la Côte d'Azur, CNRS, Laboratoire Lagrange, Bd de l'Observatoire, CS 34229, 06304 Nice cedex 4, France
[102] Mullard Space Science Laboratory, University College London, Holmbury St Mary, Dorking, Surrey RH5 6NT, UK
[103] Cosmic Dawn Center (DAWN)
[104] Universidad Politécnica de Cartagena, Departamento de Electrónica y Tecnología de Computadoras, Plaza del Hospital 1, 30202 Cartagena, Spain
[105] European University of Technology EUt+, European Union
[106] Centre for Information Technology, University of Groningen, P.O. Box 11044, 9700 CA Groningen, The Netherlands
[107] Institute of Space Sciences (ICE, CSIC), Campus UAB, Carrer de Can Magrans, s/n, 08193 Barcelona, Spain
[108] Institut d'Estudis Espacials de Catalunya (IEEC), Edifici RDIT, Campus UPC, 08860 Castelldefels, Barcelona, Spain
[109] Dipartimento di Fisica e Scienze della Terra, Università degli Studi di Ferrara, Via Giuseppe Saragat 1, 44122 Ferrara, Italy
[110] Istituto Nazionale di Fisica Nucleare, Sezione di Ferrara, Via Giuseppe Saragat 1, 44122 Ferrara, Italy
[111] ICSC - Centro Nazionale di Ricerca in High Performance Computing, Big Data e Quantum Computing, Via Magnanelli 2, Bologna, Italy
[112] INAF, Istituto di Radioastronomia, Via Piero Gobetti 101, 40129 Bologna, Italy
[113] Astronomical Observatory of the Autonomous Region of the Aosta Valley (OAVdA), Loc. Lignan 39, I-11020, Nus (Aosta Valley), Italy
[114] Department of Mathematical Physics, Institute of Physics, University of São Paulo, R. do Matão 1371, 05508-090, São Paulo, SP, Brazil
[115] Universidad de La Laguna, Dpto. Astrofísica, E-38206 La Laguna, Tenerife, Spain
[116] Universität Innsbruck, Institut für Astro- und Teilchenphysik, Technikerstr. 25/8, 6020 Innsbruck, Austria
[117] Oskar Klein Centre for Cosmoparticle Physics, Department of Physics, Stockholm University, Stockholm, SE-106 91, Sweden
[118] Astrophysics Group, Blackett Laboratory, Imperial College London, London SW7 2AZ, UK
[119] Univ. Grenoble Alpes, CNRS, Grenoble INP, LPSC-IN2P3, 53, Avenue des Martyrs, 38000 Grenoble, France
[120] Dipartimento di Fisica, Sapienza Università di Roma, Piazzale Aldo Moro 2, 00185 Roma, Italy
[121] Institut d'Astrophysique de Paris, 98bis Boulevard Arago, 75014, Paris, France
[122] ICL, Junia, Université Catholique de Lille, LITL, 59000 Lille, France
[123] Center for Astrophysics and Cosmology, University of Nova Gorica, Nova Gorica, Slovenia
[124] CERCA/ISO, Department of Physics, Case Western Reserve University, 10900 Euclid Avenue, Cleveland, OH 44106, USA
[125] Laboratoire Univers et Théorie, Observatoire de Paris, Université PSL, Université Paris Cité, CNRS, 92190 Meudon, France
[126] Departamento de Física Fundamental. Universidad de Salamanca. Plaza de la Merced s/n. 37008 Salamanca, Spain
[127] Universiteit Gent, Department of Physics and Astronomy, Proeftuinstraat 86 N3, 9000 Ghent, Belgium
[128] Konkoly Observatory, HUN-REN CSFK, MTA Centre of Excellence, Budapest, Konkoly Thege Miklós út 15-17. H-1121, Hungary
[129] MTA-CSFK Lendület Large-Scale Structure Research Group, Konkoly-Thege Miklós út 15-17, H-1121 Budapest, Hungary
[130] Université de Strasbourg, CNRS, Observatoire astronomique de Strasbourg, UMR 7550, 67000 Strasbourg, France

[131] Scuola Superiore Meridionale, Via Mezzocannone 4, 80138, Napoli, Italy
[132] Department of Physics, Astronomy and Mathematics, University of Hertfordshire, College Lane, Hatfield AL10 9AB, UK
[133] Instituto de Astrofísica e Ciências do Espaço, Faculdade de Ciências, Universidade de Lisboa, Tapada da Ajuda, 1349-018 Lisboa, Portugal
[134] Institute of Cosmology and Gravitation, University of Portsmouth, Portsmouth PO1 3FX, UK
[135] Department of Physics & Astronomy, University of California Irvine, Irvine CA 92697, USA
[136] Institute for Astronomy, University of Hawaii, 2680 Woodlawn Drive, Honolulu, HI 96822, USA
[137] Departamento Física Aplicada, Universidad Politécnica de Cartagena, Campus Muralla del Mar, 30202 Cartagena, Murcia, Spain
[138] Instituto de Física de Cantabria, Edificio Juan Jordá, Avenida de los Castros, 39005 Santander, Spain
[139] CEA Saclay, DFR/IRFU, Service d'Astrophysique, Bat. 709, 91191 Gif-sur-Yvette, France
[140] Department of Mathematics and Physics E. De Giorgi, University of Salento, Via per Arnesano, CP-I93, 73100, Lecce, Italy
[141] INFN, Sezione di Lecce, Via per Arnesano, CP-193, 73100, Lecce, Italy
[142] INAF-Sezione di Lecce, c/o Dipartimento Matematica e Fisica, Via per Arnesano, 73100, Lecce, Italy
[143] Department of Computer Science, Aalto University, PO Box 15400, Espoo, FI-00 076, Finland
[144] Ruhr University Bochum, Faculty of Physics and Astronomy, Astronomical Institute (AIRUB), German Centre for Cosmological Lensing (GCCL), 44780 Bochum, Germany
[145] DARK, Niels Bohr Institute, University of Copenhagen, Jagtvej 155, 2200 Copenhagen, Denmark
[146] Department of Physics, Centre for Extragalactic Astronomy, Durham University, South Road, Durham, DH1 3LE, UK
[147] Astrophysics Research Centre, University of KwaZulu-Natal, Westville Campus, Durban 4041, South Africa
[148] School of Mathematics, Statistics & Computer Science, University of KwaZulu-Natal, Westville Campus, Durban 4041, South Africa
[149] Department of Physics and Astronomy, Vesilinnantie 5, University of Turku, 20014 Turku, Finland
[150] Finnish Centre for Astronomy with ESO (FINCA), Quantum, Vesilinnantie 5, University of Turku, 20014 Turku, Finland
[151] Serco for European Space Agency (ESA), Camino bajo del Castillo, s/n, Urbanizacion Villafranca del Castillo, Villanueva de la Cañada, 28692 Madrid, Spain
[152] ARC Centre of Excellence for Dark Matter Particle Physics, Melbourne, Australia
[153] Centre for Astrophysics & Supercomputing, Swinburne University of Technology, Hawthorn, Victoria 3122, Australia
[154] Department of Physics and Helsinki Institute of Physics, Gustaf Hällströmin katu 2, University of Helsinki, 00014 Helsinki, Finland
[155] Ohio University, Physics & Astronomy Department,1 Ohio University, Athens, OH 45701, USA
[156] Brazilian Center for Research in Physics (CBPF), Dr. Xavier Sigaud st. 150, zip 22290-180, Rio de Janeiro, RJ, Brazil
[157] Institute for Theoretical Particle Physics and Cosmology (TTK), RWTH Aachen University, 52056 Aachen, Germany
[158] IRFU, CEA, Université Paris-Saclay 91191 Gif-sur-Yvette Cedex, France
[159] INAF-Osservatorio Astrofisico di Arcetri, Largo E. Fermi 5, 50125, Firenze, Italy
[160] Centro de Astrofísica da Universidade do Porto, Rua das Estrelas, 4150-762 Porto, Portugal
[161] HE Space for European Space Agency (ESA), Camino bajo del Castillo, s/n, Urbanizacion Villafranca del Castillo, Villanueva de la Cañada, 28692 Madrid, Spain
[162] Dipartimento di Fisica "G. Occhialini", Università degli Studi di Milano Bicocca, Piazza della Scienza 3, 20126 Milano, Italy
[163] Department of Astrophysics, University of Zurich, Winterthurerstrasse 190, 8057 Zurich, Switzerland
[164] Space physics and astronomy research unit, University of Oulu, Pentti Kaiteran katu 1, FI-90014 Oulu, Finland
[165] Theoretical astrophysics, Department of Physics and Astronomy, Uppsala University, Box 524, 751 20 Uppsala, Sweden
[166] Mathematical Institute, University of Leiden, Einsteinweg 55, 2333 CA Leiden, The Netherlands
[167] School of Physical Sciences, The Open University, Milton Keynes, MK7 6AA, UK
[168] Institute of Astronomy, University of Cambridge, Madingley Road, Cambridge CB3 0HA, UK
[169] Univ. Lille, CNRS, Centrale Lille, UMR 9189 CRIStAL, 59000 Lille, France
[170] Kobayashi-Maskawa Institute for the Origin of Particles and the Universe, Nagoya University, Chikusa-ku, Nagoya, 464-8602, Japan
[171] Department of Astrophysical Sciences, Peyton Hall, Princeton University, Princeton, NJ 08544, USA
[172] Fakultät für Physik, Universität Bielefeld, Postfach 100131, 33501 Bielefeld, Germany
[173] School of Mathematics, Statistics and Physics, Newcastle University, Herschel Building, Newcastle-upon-Tyne, NE1 7RU, UK
[174] Department of Physics and Astronomy, University of British Columbia, Vancouver, BC V6T 1Z1, Canada

⋆ e-mail: mario.radovich@inaf.it